

The Durham/UKST Galaxy Redshift Survey - IV. Redshift Space Distortions in the 2-Point Correlation Function.

A. Ratcliffe¹, T. Shanks¹, R. Fong¹ and Q.A. Parker²

¹*Physics Department, University of Durham, South Road, Durham, DH1 3LE.*

²*Anglo-Australian Observatory, Coonabarabran, NSW 2357, Australia.*

22 January 2018

ABSTRACT

We have investigated the redshift space distortions in the optically selected Durham/UKST Galaxy Redshift Survey using the 2-point galaxy correlation function perpendicular and parallel to the observer’s line of sight, $\xi(\sigma, \pi)$. We present results for the real space 2-point correlation function, $\xi(r)$, by inverting the optimally estimated projected correlation function, which is obtained by integration of $\xi(\sigma, \pi)$, and find good agreement with other real space estimates. On small, non-linear scales we observe an elongation of the constant $\xi(\sigma, \pi)$ contours in the line of sight direction. This is due to the galaxy velocity dispersion and is the common “Finger of God” effect seen in redshift surveys. Our result for the one-dimensional pairwise rms velocity dispersion is $\langle w^2 \rangle^{1/2} = 416 \pm 36 \text{ km s}^{-1}$ which is consistent with those from recent redshift surveys and canonical values, but inconsistent with SCDM or LCDM models. On larger, linear scales we observe a compression of the $\xi(\sigma, \pi)$ contours in the line of sight direction. This is due to the infall of galaxies into overdense regions and the Durham/UKST data favours a value of $(\Omega^{0.6}/b) \sim 0.5$, where Ω is the mean mass density of the Universe and b is the linear bias factor which relates the galaxy and mass distributions. Comparison with other optical estimates yield consistent results, with the conclusion that the data does not favour an unbiased critical-density universe.

Key words: galaxies: clusters – galaxies: general – cosmology: observations – large-scale structure of Universe.

1 INTRODUCTION

The use of redshifts as distance estimates is commonplace in surveys which map the galaxy distribution of the Universe. While redshifts are both quick and easy to acquire, they do not generally reflect the true distance to the galaxy because of the galaxy’s own peculiar velocity with respect to the Hubble flow. Therefore, the observed clustering pattern will be imprinted with the galaxy peculiar velocity field along the observer’s line of sight direction. While at first this would appear to be highly problematic for the use and understanding of the measured clustering statistics, these so-called redshift space distortions can be used to estimate some important cosmological parameters describing the dynamics of the Universe (e.g. Peebles 1980; Kaiser 1987).

We will be investigating these redshift space distortions using the spatial 2-point correlation function, ξ , and denote a real space separation by r and a redshift space separation by s . Non-linear and linear effects will be competing on all scales but for the most part we take the simplifying

assumption that non-linear effects dominate on small scales ($< 10h^{-1}\text{Mpc}$), whereas linear effects dominate on larger scales ($> 10h^{-1}\text{Mpc}$). Although this is a slightly naive approach we use N-body simulations and mock catalogues to guide us in determining the accuracy of the modelling involved.

The initial clustering results, redshift maps, etc. of the Durham/UKST Galaxy Redshift Survey were summarized in the first paper of this series (Ratcliffe et al. 1996a). In this paper we present a detailed analysis of the redshift space distortions in the 2-point correlation function as estimated from this optically selected survey. We briefly describe our survey in Section 2. Section 3 gives a qualitative description of the effects of the redshift space distortions on the 2-point correlation function. In Section 4 we describe and test methods of obtaining the real space correlation function from redshift space estimates. In Section 5 we describe non-linear effects and estimate the one-dimensional rms galaxy pairwise velocity dispersion. Linear infall effects are described in Section 6 and an estimate of $\Omega^{0.6}/b$ is obtained. The re-

sults of this analysis are discussed and compared with other redshift surveys and models of structure formation in Section 7. Finally, we summarize our conclusions in Section 8.

2 THE DURHAM/UKST GALAXY REDSHIFT SURVEY

The Durham/UKST Galaxy Redshift Survey was constructed using the FLAIR fibre optic system (Parker & Watson 1995) on the 1.2m UK Schmidt Telescope at Sidling Spring, Australia. This survey uses the astrometry and photometry from the Edinburgh/Durham Southern Galaxy Catalogue (EDSGC; Collins, Heydon-Dumbleton & MacGillivray 1988; Collins, Nichol & Lumsden 1992) and was completed in 1995 after a 3-yr observing programme. The survey itself covers a $\sim 20^\circ \times 75^\circ$ area centered on the South Galactic Pole (60 UKST plates) and is sparse sampled at a rate of one in three of the galaxies to $b_J \simeq 17$ mag. The resulting survey contains ~ 2500 redshifts, probes to a depth greater than $300h^{-1}\text{Mpc}$, with a median depth of $\sim 150h^{-1}\text{Mpc}$, and surveys a volume of space $\sim 4 \times 10^6 (h^{-1}\text{Mpc})^3$.

The survey is >75 per cent complete to the nominal magnitude limit of $b_J = 17.0$ mag. This incompleteness was mainly caused by poor observing conditions, intrinsically low throughput fibres and other various observational effects. In a comparison with ~ 150 published galaxy velocities (Peterson et al. 1986; Fairall & Jones 1988; Metcalfe et al. 1989; da Costa et al. 1991) our measured redshifts had negligible offset and were accurate to $\pm 150 \text{ km s}^{-1}$. The scatter in the EDSGC magnitudes has been estimated at ± 0.22 mags (Metcalfe, Fong & Shanks 1995) for a sample of ~ 100 galaxies. This scatter has been confirmed by a preliminary analysis of a larger sample of high quality CCD photometry. All of these observational details are discussed further in a forthcoming data paper (Ratcliffe et al., in preparation).

3 REDSHIFT SPACE DISTORTIONS

We investigate the effects of redshift space distortions by estimating the spatial 2-point correlation function, ξ , as a function of the two variables σ and π . These are the separations perpendicular (σ) and parallel (π) to the line of sight. The specific definitions of σ and π we use were given in Ratcliffe et al. (1996c), hereafter Paper III. However, we found that our results do not depend significantly on their exact form.

Galaxy peculiar velocities cause an otherwise isotropic real space correlation function to become anisotropic when observed in redshift space. The degree of anisotropy measures the low-order moments of the peculiar velocity distribution function (e.g. Peebles 1980). On small, non-linear scales ($< 10h^{-1}\text{Mpc}$) the velocity dispersion of galaxies in virialised regions dominates the anisotropy, causing an elongation in the contours of constant ξ along the line of sight direction. This is the well-known ‘‘Finger of God’’ effect seen in redshift surveys and allows one to estimate the one-dimensional pairwise rms velocity dispersion of galaxies, $\langle w^2 \rangle^{1/2}$ (e.g. Davis & Peebles 1983). On larger, more linear scales ($> 10h^{-1}\text{Mpc}$) the infall of galaxies into overdense

regions dominates, causing a compression of the ξ contours in the line of sight direction (Kaiser 1987). This effect allows a measurement of $\Omega^{0.6}/b$. While our division of the non-linear and linear regimes is slightly naive, we will be guided by CDM mock catalogues to determine the accuracy of the modelling in the different regions.

3.1 The Redshift Space 2-Point Correlation Function, $\xi(\sigma, \pi)$

We have estimated $\xi(\sigma, \pi)$ using the optimal methods determined empirically in Paper III. Briefly, this involves distributing a random and homogeneous catalogue with the same angular and radial selection functions as the original survey. One then cross correlates data-data, data-random and random-random pairs, binning them as a function of separation (in this case σ and π). As a result of testing Monte Carlo mock catalogues drawn from CDM N -body simulations we found that the estimator and weighting combination which most accurately traced the actual ξ and also produced the minimum variance in ξ was the estimator of Hamilton (1993) and the weighting of Efstathiou (1988). All of these techniques and the biases in them are discussed at length in Paper III and we refer the interested reader there.

In Figs. 1 and 2 we show contour plots of constant ξ as a function of σ and π . On both of these figures we adopt the following conventions: solid lines denote $\xi > 1$ with $\Delta\xi = 1$; short-dashed lines denote $0 < \xi < 1$ with $\Delta\xi = 0.1$; and long-dashed lines denote $\xi < 0$ with $\Delta\xi = 0.1$. For reference, the contours $\xi = 1$ and 0 are in thick bold and the regularly spaced thin bold lines show an isotropic correlation function for comparison. When the plotted scale is log-log the binning size is $0.2dex$, when it is linear-linear the binning is $1.0h^{-1}\text{Mpc}$. In both cases no formal smoothing has been applied.

3.2 Results from the CDM models

We have calculated the $\xi(\sigma, \pi)$ results from two different CDM models (Efstathiou et al. 1985; Gaztañaga & Baugh 1995; Eke et al. 1996): standard CDM with $\Omega h = 0.5$, $b = 1.6$ (SCDM); and CDM with $\Omega h = 0.2$, $b = 1$ and a cosmological constant ($\Lambda = 0.8$) to ensure a spatially flat cosmology (LCDM). In Fig. 1(a) we show the average $\xi(\sigma, \pi)$ calculated directly from the 9 SCDM N -body simulations which were available to us, while Fig. 1(b) shows the average from the 5 available LCDM simulations. Given that these simulations are fully volume limited with a well-defined mean density there are no problems with estimator/weighting schemes and we estimate ξ using the methods described in Paper III for this case. For simplicity, we also use the distant observer approximation (i.e. we imagine placing the N -body cube at a large distance from the observer) and therefore the line of sight direction can be assumed to be one specific direction. We choose this to be the z -direction and hence $\sigma = \sqrt{x^2 + y^2}$, $\pi = z$ and the bins are cylindrical shells.

Fig. 1(a) shows that the small scale velocity dispersion in the SCDM model dominates the whole plot, elongating the contours even on large scales ($\pi > 10h^{-1}\text{Mpc}$). The $\xi = 1$ contour cuts the σ axis between $4.5\text{--}5.0h^{-1}\text{Mpc}$, which agrees well with the real space correlation length of

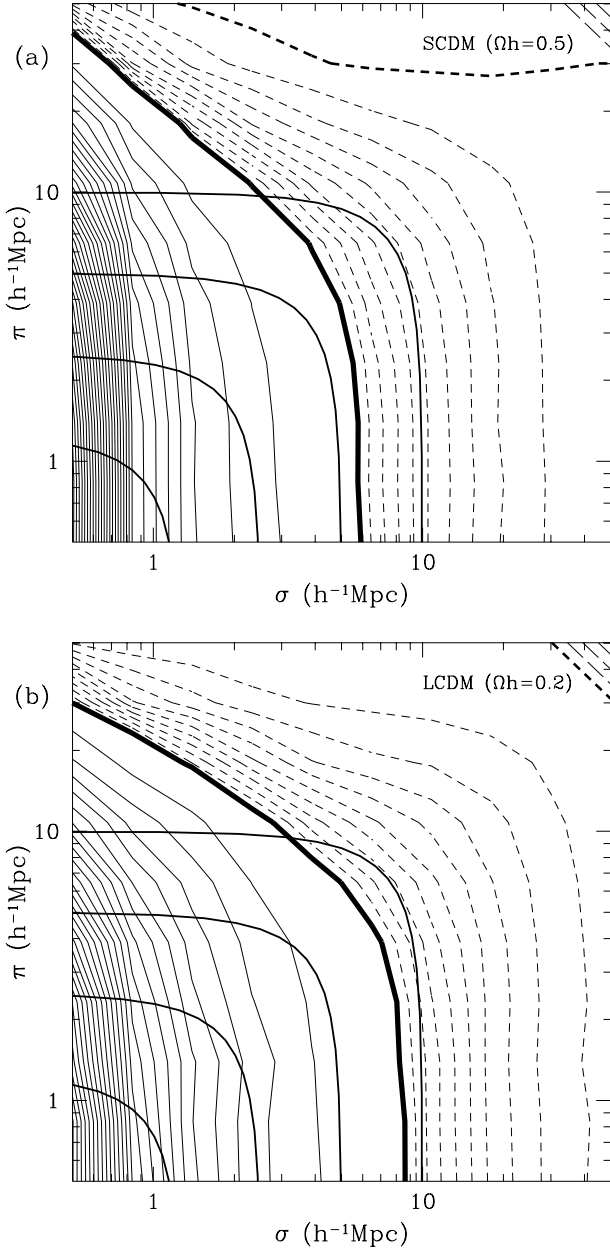


Figure 1. The results of $\xi(\sigma, \pi)$ calculated directly from N -body simulations of two different CDM models. Fig. (a) shows the average of the 9 available SCDM simulations, while Fig. (b) shows the average of the 5 available LCDM simulations. The different types of contours are described in detail in the text of Section 3.1. It is clear that the elongation of the contours in the line of sight (π) direction, caused by the non-linear galaxy velocity dispersion, dominates the SCDM model. A similar effect is seen in the LCDM model, although at a lower level.

$\sim 5.0h^{-1}\text{Mpc}$ estimated in Paper III. While there is a strong signal to be modelled for the non-linear results, it is very doubtful that any useful information will be obtained for the linear results of the SCDM model without a more sophisticated approach than is attempted here.

Fig. 1(b) shows that the small scale velocity dispersion in the LCDM model is also the dominant feature on this

plot, albeit less pronounced than the SCDM model. Indeed, there is possible evidence of a flattening in the π direction on $\sim 20h^{-1}\text{Mpc}$ scales. The $\xi = 1$ contour cuts the σ axis between $6.0\text{--}6.5h^{-1}\text{Mpc}$, which again agrees well with the real space correlation length of $\sim 6.0h^{-1}\text{Mpc}$ estimated in Paper III. Again, there is a strong signal for the non-linear results to model but this time it appears possible that a sensible linear result could be obtained from the LCDM model (see Section 6).

3.3 Results from the Durham/UKST Survey

In Fig. 2 we show the results of $\xi(\sigma, \pi)$ from the Durham/UKST survey as calculated using the optimal methods and magnitude limits described in Ratcliffe et al. (1996b) and Paper III. As mentioned in Section 3.1 this includes the estimator of Hamilton (1993) and the weighting of Efstathiou (1988). It is obvious that the noise levels for the data are significantly higher than those of the N -body simulations. Given the differences in signal between the N -body simulations and the redshift survey this was to be expected. As an aside, we note that the CDM mock catalogues used later in this paper have similar noise levels to the data in plots like these. Fig. 2 shows that the non-linear velocity dispersion does not dominate the whole plot (unlike the CDM models of Fig. 1) and there is no significant elongation beyond $\pi \sim 5\text{--}10h^{-1}\text{Mpc}$. Also, on larger scales than these a visible compression of the contours in the π direction is seen. Therefore, we are confident that believable non-linear and linear results can be obtained from the Durham/UKST survey using the approach attempted here.

4 THE REAL SPACE 2-POINT CORRELATION FUNCTION

We define the projected 2-point correlation function, $w_v(\sigma)$, by (e.g. Peebles 1980)

$$w_v(\sigma) = \int_{-\infty}^{\infty} \xi(\sigma, \pi) d\pi, \quad (1)$$

$$= 2 \int_0^{\infty} \xi(\sqrt{\sigma^2 + \pi^2}) d\pi, \quad (2)$$

where $\xi(\sqrt{\sigma^2 + \pi^2})$ is the real space correlation function. We calculate $w_v(\sigma)$ using

$$w_v(\sigma) = 2 \int_0^{\pi_{cut}} \xi(\sigma, \pi) d\pi, \quad (3)$$

where the noise in $\xi(\sigma, \pi)$ at very large scales makes us truncate the integral at some finite limit π_{cut} . In practice we use a π_{cut} of $30h^{-1}\text{Mpc}$ and our results are insensitive to raising this value.

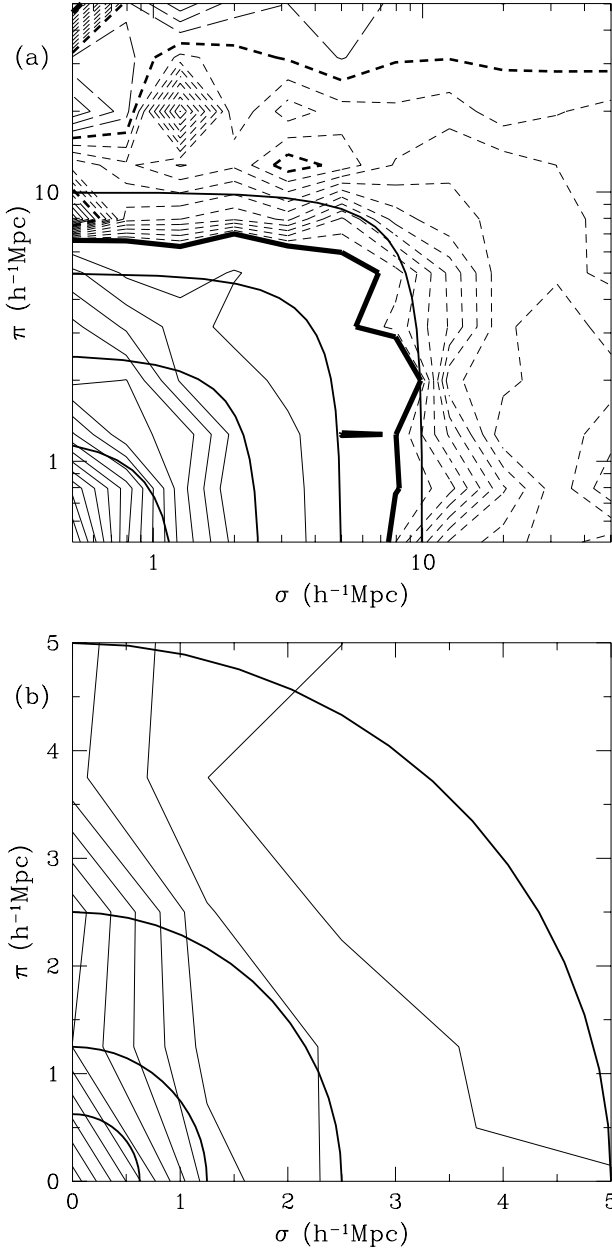


Figure 2. The results of $\xi(\sigma, \pi)$ estimated from the Durham/UKST survey using the optimal methods involving the estimator of Hamilton (1993) and the weighting of Efstathiou (1988). Fig. (a) plots the results on a log-log scale to emphasize the large scale features, while Fig. (b) plots the results on a linear-linear scale to emphasize the small scale features. The different types of contours are described in detail in the text of Section 3.1. One immediately sees that the noise levels in these diagrams are significantly higher than those of the N -body simulations shown in Fig. 1. These contour plots also show that the non-linear velocity dispersion elongates the contours in the line of sight (π) direction out to $5\text{--}10h^{-1}\text{Mpc}$. However, on larger scales there is evidence for a measurable flattening of the contours in the π direction.

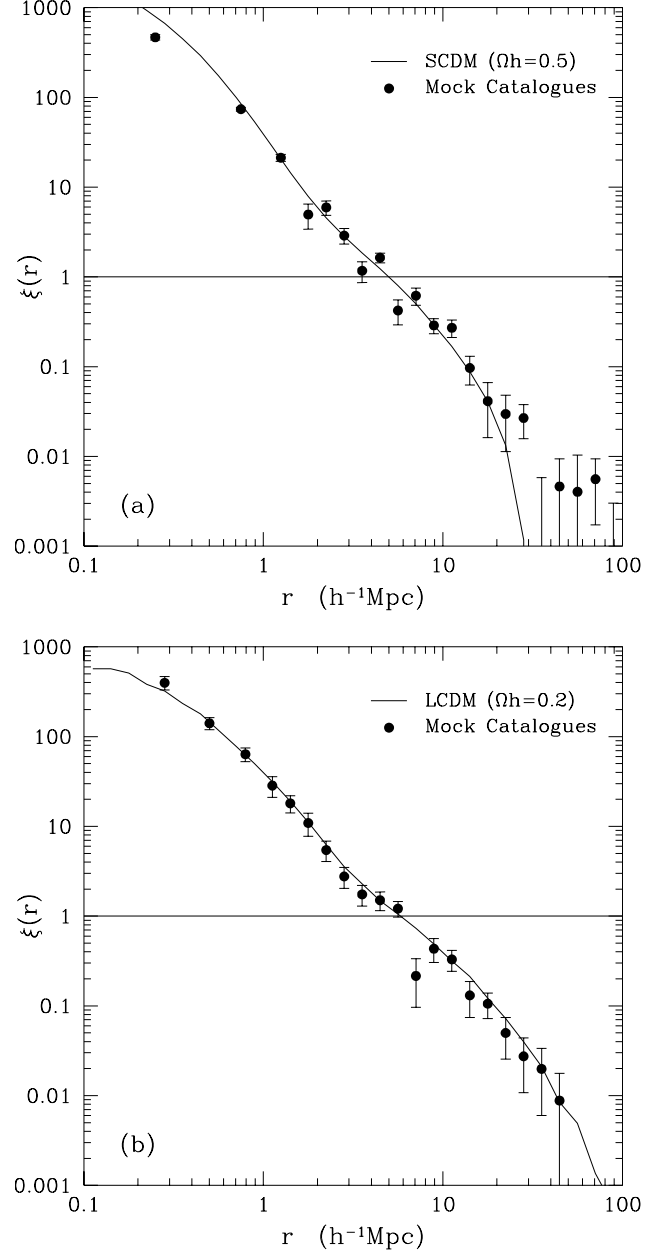


Figure 3. Testing the methods of estimating $\xi(r)$ using the Abel inversion of $w_v(\sigma)$ from (a) the SCDM and (b) the LCDM mock catalogues. We show a comparison of the actual $\xi(r)$ calculated directly from N -body simulations (solid line) with the average $\xi(r)$ obtained from the mock catalogues (solid symbols). These points came from taking each catalogue's optimally estimated $\xi(\sigma, \pi)$, performing the integral in equation 3 to give a set of $w_v(\sigma)$'s, then carrying out the summations in equation 5 to give a set of $\xi(r)$'s and finally averaging to obtain the results. The error bars show the 1σ standard deviation on this mean assuming that each mock catalogue provides an independent estimate of $\xi(r)$.

As we have discussed in Section 3, any catalogue which uses redshifts to estimate distances suffers from the effects of galaxy peculiar velocities. Therefore, only the redshift space 2-point correlation function, $\xi(s)$, is directly observable from a redshift survey. However, in terms of measuring and comparing the clustering properties of the galaxy distribution with models of structure formation, the object of fundamental interest is the real space 2-point correlation function, $\xi(r)$. While $\xi(r)$ is not directly observable from a redshift survey we will see that it is possible to estimate it in an indirect manner. In this context we follow on from results presented in Paper III.

4.1 The Projected 2-Point Correlation Function

Our methods of estimating $w_v(\sigma)$ were tested in Paper III where the results from the Durham/UKST survey were first presented (using the optimal methods mentioned in Section 3.3 for calculating ξ). We then went on to model $w_v(\sigma)$ using a power law for $\xi(r) = (r_0/r)^\gamma$ and estimated the real space correlation length, $r_0 = 5.1 \pm 0.3$, and slope, $\gamma = 1.6 \pm 0.1$. In this section, rather than assume a power law form, we consider a direct inversion of equation 2 to give $\xi(r)$.

4.2 Abel Inversion

Equation 2 can be mathematically inverted using the generalized Abel equation to give (e.g. Lilje & Efstathiou 1988)

$$\xi(r) = -\frac{1}{\pi} \int_r^\infty \frac{d[w_v(\sigma)]}{d\sigma} \frac{d\sigma}{\sqrt{\sigma^2 - r^2}}. \quad (4)$$

Saunders, Rowan-Robinson & Lawrence (1992) consider the case when the data is logarithmically binned and $w_v(\sigma)$ then takes the form of a series of step functions, $w_v(\sigma_i) = w_i$, with logarithmic spacing centered on σ_i . They then linearly interpolate between each w_v point to get around singularities in the integral. In this case the $d[w_v(\sigma)]/d\sigma$ factor simplifies to a constant value for each pair of σ_i spacings. The rest of the integral can be evaluated to give $\xi(r)$ at $r = \sigma_i$

$$\xi(\sigma_i) = -\frac{1}{\pi} \sum_{j \geq i} \left[\frac{w_{j+1} - w_j}{\sigma_{j+1} - \sigma_j} \right] \ln \left(\frac{\sigma_{j+1} + \sqrt{\sigma_{j+1}^2 - \sigma_i^2}}{\sigma_j + \sqrt{\sigma_j^2 - \sigma_i^2}} \right). \quad (5)$$

We test this method using mock catalogues drawn from the SCDM and LCDM N -body simulations. These mock catalogues have the same angular/radial selection functions and completeness rates as the Durham/UKST survey and their construction was described in detail in Paper III. We selected the mock catalogues to sample independent volumes of the simulations, giving a total of 18 and 15 to analyse from the SCDM and LCDM simulations, respectively. The results of $w_v(\sigma)$ from these two sets of mock catalogues were presented in Paper III and Fig. 3 shows the results of applying equation 5 to this $w_v(\sigma)$ data. The solid line shows the actual $\xi(r)$ calculated directly from the N -body simulations and therefore denotes the answer we are trying to obtain. The solid symbols show the average $\xi(r)$ obtained from the mock catalogues by taking each catalogue's optimally estimated $\xi(\sigma, \pi)$, performing the integral in equation 3 to give a set of $w_v(\sigma)$'s, then carrying out the summations in equation 5 to give a set of $\xi(r)$'s and finally averaging. The error

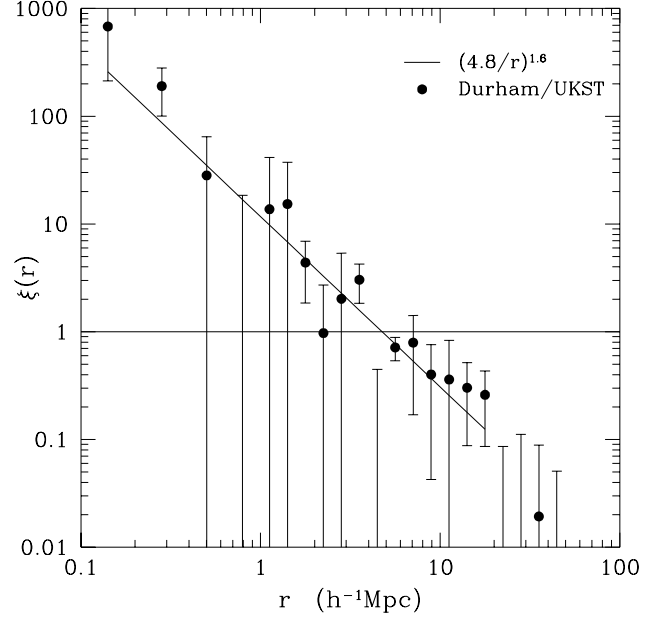


Figure 4. Estimates of $\xi(r)$ from the Durham/UKST survey obtained by Abel inversion of $w_v(\sigma)$. The points are calculated by taking the optimally estimated $\xi(\sigma, \pi)$ from Fig. 2, evaluating the integral in equation 3 to give $w_v(\sigma)$ and then inverting this with equation 5 to produce $\xi(r)$. The solid line shows the best fitting power law to the estimated $\xi(r)$ in the indicated range.

bars show the 1σ standard deviation on this mean assuming that each mock catalogue provides an independent estimate of $\xi(r)$.

The SCDM results in Fig. 3(a) show that the mock catalogues reproduce the actual $\xi(r)$ quite well out to $\sim 25h^{-1}\text{Mpc}$ scales (with some degree of scatter about the answer). On scales larger than this $\xi(r)$ is zero and therefore there is no signal to invert, other than the noise in $\xi(\sigma, \pi)$. The LCDM results in Fig. 3(b) show that the mock catalogues reproduce the actual $\xi(r)$ very well out to $\sim 40h^{-1}\text{Mpc}$ (apart from the point at $\sim 7h^{-1}\text{Mpc}$ which is caused by a couple of negative $\xi(r)$ points produced in the inversion process). Overall, we see that this method of inversion does reproduce the actual $\xi(r)$ and its features quite well, albeit with considerable scatter in places.

This method of estimating $\xi(r)$ is applied to the Durham/UKST survey $\xi(\sigma, \pi)$ data of Fig. 2. The $w_v(\sigma)$ results were shown in Paper III and are used in equation 5 to produce the $\xi(r)$ shown in Fig. 4. The error bars on this plot are obtained by splitting the Durham/UKST survey into 4 quadrants, applying the method to each quadrant and then estimating a standard deviation of these results. These error bars are of a similar size to those estimated on an individual LCDM mock catalogue. The solid line shows the minimum χ^2 fit of a power law $\xi(r) = (r_0/r)^\gamma$ in the $0.1\text{--}20h^{-1}\text{Mpc}$ region. The best fit parameters were $r_0 = 4.8 \pm 0.5h^{-1}\text{Mpc}$ and $\gamma = 1.6 \pm 0.3$, which gave a χ^2 of ~ 8 for 15 degrees of freedom. Note that the negative point at $\sim 4.5h^{-1}\text{Mpc}$ was removed from this χ^2 statistic to avoid biasing the fit. Errors on these parameters come from the appropriate $\Delta\chi^2$ contour about the minimum. However, given the correlated nature of these points we anticipate that our quoted errors are more

than likely an underestimate. This should be adequate for the simple comparison done here.

4.3 Richardson-Lucy Inversion

Richardson-Lucy inversion has recently been made popular in large-scale structure applications by Baugh & Efstathiou (1993) and here we apply it to estimate $\xi(r)$ from $w_v(\sigma)$. Equation 2 can be re-written as

$$w_v(\sigma) = \int_{\sigma}^{\infty} \xi(r) \left(\frac{2r}{\sqrt{r^2 - \sigma^2}} \right) dr, \quad (6)$$

by changing the variable of integration from π to r . If we then define

$$K(\sigma, r) = 0 \quad \text{for } 0 < r < \sigma, \quad (7)$$

$$= \frac{2r}{\sqrt{r^2 - \sigma^2}} \quad \text{for } \sigma < r < \infty, \quad (8)$$

our integral becomes

$$w_v(\sigma) = \int_0^{\infty} \xi(r) K(\sigma, r) dr, \quad (9)$$

which is in the form of a Fredholm integral equation of the first kind

$$\phi(x) = \int_a^b \psi(t) P(x|t) dt, \quad (10)$$

where $\phi(x)$ is the known (or observed) function, $\psi(t)$ is the unknown function and $P(x|t)$ is the kernel of the integral equation. Therefore, equation 6 can be numerically inverted using the method developed independently by Richardson (1972) and Lucy (1974). Basically, one guesses an initial form for $\psi(t)$, predicts $\phi(x)$ and uses this to update the original $\psi(t)$. This iteration continues and after n iterates

$$\phi^n(x) = \int_a^b \psi^n(t) P(x|t) dt, \quad (11)$$

with the next iterate of $\psi(t)$ given by

$$\psi^{n+1}(t) = \psi^n(t) \frac{\int_a^b \frac{\tilde{\phi}(x)}{\phi^n(x)} P(x|t) dx}{\int_a^b P(x|t) dx}, \quad (12)$$

where $\tilde{\phi}(x)$ is the actual observed function. To apply this method to the logarithmically binned $w_v(\sigma)$ data the integrals in equations 11 and 12 are approximated by the following summations

$$w_v^n(\sigma_j) = \sum_{i=1}^N \xi^n(r_i) K(\sigma_j, r_i) r_i \Delta \ln r, \quad (13)$$

$$\xi^{n+1}(r_i) = \xi^n(r_i) \frac{\sum_{j=1}^M \frac{\tilde{w}_v(\sigma_j)}{w_v^n(\sigma_j)} K(\sigma_j, r_i) \sigma_j \Delta \ln \sigma}{\sum_{j=1}^M K(\sigma_j, r_i) \sigma_j \Delta \ln \sigma}, \quad (14)$$

where M is the number of $w_v(\sigma)$ bins and $N = M/2$ is the number of $\xi(r)$ bins. Our spacing in σ is $\Delta \lg \sigma = 0.1$ and hence our spacing in r is $\Delta \lg r = 0.2$. Obviously one cannot get back more data points than are put in and $N \leq M$. In general, our choice of $N = M/2$ should assure a fairly smooth answer.

There are two points worth noting about Richardson-Lucy algorithms. Firstly, there is no constraint on how many

iterations are required for convergence to a stable answer. Therefore, there is no specific rule to know when to stop iterating. Too many iterations will cause convergence to the small scale noise features in the data, while too few implies that the results have not yet converged to the larger scale signal. Experience with Richardson-Lucy techniques shows that ~ 10 iterations are generally required (e.g. Lucy 1994). Secondly, this method assumes that the function $\psi(t) \geq 0$. This is not always the case for our function $\xi(r)$. However, this is not too worrying as $\xi(r)$ is only likely to go negative on large scales when it is nearly zero, this is where our inversion process will be least believable anyway. Also, other authors (e.g. Baugh & Efstathiou 1993; Baugh 1996) have applied similar inversion techniques to the angular correlation function to estimate the power spectrum (always positive) and real space correlation function (negative tail) and find very consistent results.

We again test these methods using the SCDM and LCDM mock catalogues. Fig. 5 shows the results of applying equations 13 and 14 to the $w_v(\sigma)$ data. Again, the solid line shows the actual $\xi(r)$ calculated directly from the N -body simulations and the solid symbols show the $\xi(r)$ obtained from the mock catalogues by individually inverting $w_v(\sigma)$ with the iteration process and averaging at the end. The circles show the results on stopping after 10 iterations, while the triangles show the results after 20 iterations. The results were found to be independent of the initial form of $\xi(r)$, therefore a simple power law was used. The error bars show the 1σ standard deviation on this mean assuming that each mock catalogue provides an independent estimate of $\xi(r)$.

The SCDM results in Fig. 5(a) show that the mock catalogues reproduce the actual $\xi(r)$ very well out to $\sim 30h^{-1}\text{Mpc}$ scales. On larger scales noise in the data dominates and this is the limit where we believe our inversion technique. It appears that the results do not change very much with further iteration. The LCDM results in Fig. 5(b) show a similar form to those of the SCDM mock catalogues and reproduce the actual $\xi(r)$ very well out to $\sim 40h^{-1}\text{Mpc}$ scales. Again, on larger scales noise in the data dominates and this is our believable inversion limit. Further iteration does not damage the stability of the inversion although the results do become less smooth. We note that this inversion technique does not appear to do well at the end-points of the integration range, this is an artifact of the finite integration range (which assumes that the signal is zero outside of this range) and the large bins used in the summations. Therefore, our results could be improved by interpolating between the $w_v(\sigma)$ points and then inverting this function given that we could calculate it at many points. Given the uncertainties involved in $\xi(\sigma, \pi)$ this is not attempted here. Overall, this method of inversion reproduces the actual $\xi(r)$ and its features very well and is arguably smoother than the Abel inversion. However, this is offset by only having an estimate at half the number of r points.

This method of estimating $\xi(r)$ is applied to the Durham/UKST survey $\xi(\sigma, \pi)$ data of Fig. 2. The $w_v(\sigma)$ results were shown in Paper III and are used in equations 13 and 14 to produce the $\xi(r)$ shown in Fig. 6. The error bars on this plot are obtained by splitting the Durham/UKST survey into 4 quadrants, applying the method to each quadrant and then estimating a standard deviation of these results.

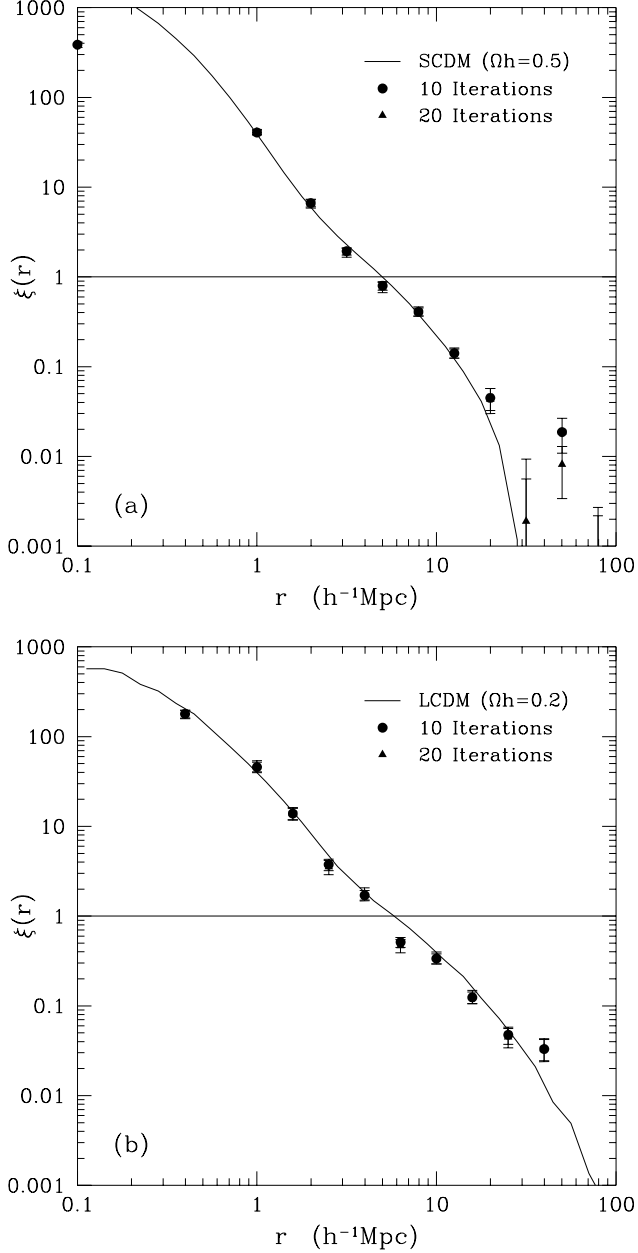


Figure 5. Testing the methods of estimating $\xi(r)$ using Richardson-Lucy inversion of $w_v(\sigma)$ from (a) the SCDM and (b) the LCDM mock catalogues. We show a comparison of the actual $\xi(r)$ calculated directly from N -body simulations (solid line) with the average $\xi(r)$ obtained from the mock catalogues (solid symbols). These points came from taking each catalogue's optimally estimated $\xi(\sigma, \pi)$, performing the integral in equation 3 to give a set of $w_v(\sigma)$'s, then carrying out the iteration between equations 13 and 14 to give a set of $\xi(r)$'s and finally averaging to obtain the results. The circles show the results on stopping after 10 iterations, while the triangles show the same results after 20 iterations. The error bars show the 1σ standard deviation on this mean assuming that each mock catalogue provides an independent estimate of $\xi(r)$.

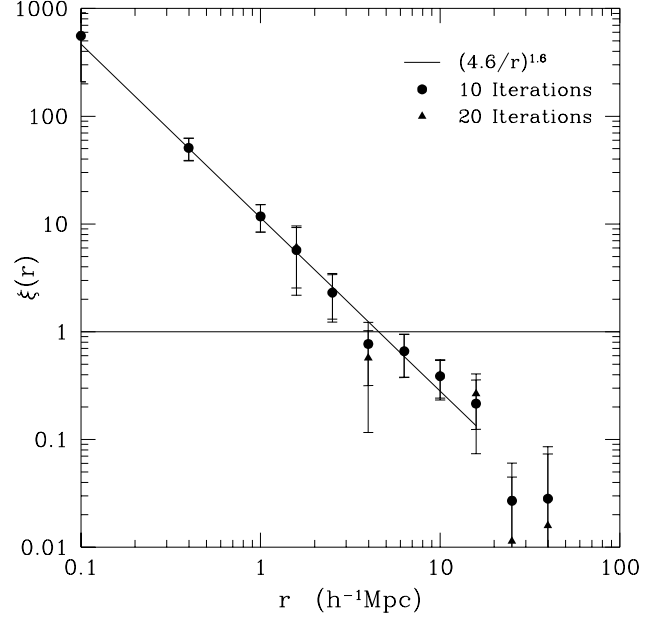


Figure 6. Estimates of $\xi(r)$ from the Durham/UKST survey obtained by Richardson-Lucy inversion of $w_v(\sigma)$. The solid points are calculated by taking the optimally estimated $\xi(\sigma, \pi)$ from Fig. 2, evaluating the integral in equation 3 to give $w_v(\sigma)$ and then inverting using the iteration process involving equations 13 and 14 to produce $\xi(r)$. The circles show the results on stopping after 10 iterations, while the triangles show the results after 20 iterations. The solid line shows the best fitting power law to the estimated $\xi(r)$ in the indicated range.

These error bars are of a similar size to those estimated on an individual LCDM mock catalogue. It can be seen that further iteration does not improve the results, in fact it makes them slightly less smooth. The solid line shows the minimum χ^2 fit of a power law $\xi(r) = (r_0/r)^\gamma$ in the 0.1 - $20h^{-1}$ Mpc region. The best fit parameters were $r_0 = 4.6 \pm 0.6h^{-1}$ Mpc and $\gamma = 1.6 \pm 0.1$, which gave a χ^2 of ~ 2 for 8 degrees of freedom. Note that the point at $\sim 4.5h^{-1}$ Mpc (which was negative for the Abel inversion) is still low. However, it does not bias the fit because the larger binning in this method has essentially averaged over it. Errors on these parameters come from the appropriate $\Delta\chi^2$ contour about the minimum. We make a similar comment to before about the correlated nature of these points implying an underestimated error on these parameters. Again, this should be adequate for the simple comparison done here.

4.4 Discussion

Before discussing the results in detail we make a few comments about the inversion methods themselves. Firstly, given that the Abel inversion is a point by point process, the noise in $w_v(\sigma)$ is also inverted. This is similar to what is seen if the Richardson-Lucy inversion is allowed to continue iterating, namely it converges to the small scale noise features in the data. Therefore, the smoothest answer is produced by the Richardson-Lucy inversion after ~ 10 iterations. Secondly, both of these methods do not do particularly well at the end points of the integration range. On the large scales

this was to be expected as it is here that the signal is almost zero and the noise dominates. On small scales this is due to a combination of the cutoff at $0.1h^{-1}\text{Mpc}$ and the approximation of the integrals in equations 13 and 14 by finite summations with quite large bins. Thirdly, as a consistency check on the Richardson-Lucy method, we have examined the $w_v(\sigma)$ produced by the iteration procedure. We find that this $w_v(\sigma)$ is in excellent agreement with the original one obtained directly from the data. Finally, while we have only shown the results of testing these inversion methods on the CDM mock catalogues, we also tested these techniques on other data sets. We constructed simple power laws in $\xi(\sigma, \pi)$ and also more complicated power laws with break features, both with and without noise. The methods passed all of these tests and therefore we are confident of applying them to the Durham/UKST survey to give believable results for $\xi(r)$.

We now discuss the $\xi(r)$ results obtained from the Durham/UKST survey. Figs. 4 and 6 show that the results from these two different inversion techniques agree well. The Abel method is generally noisier than the Richardson-Lucy method but has $\xi(r)$ estimates at twice as many points. Comparing the power law fits gives very good agreement in both correlation length and slope: $r_0 = 4.8 \pm 0.5 h^{-1}\text{Mpc}$ and $\gamma = 1.6 \pm 0.3$ for the Abel method, and $r_0 = 4.6 \pm 0.6 h^{-1}\text{Mpc}$ and $\gamma = 1.6 \pm 0.1$ for the Richardson-Lucy method. These values are also in good agreement with those estimated by modelling $\xi(r)$ as a power law and fitting this model to $w_v(\sigma)$, namely $r_0 = 5.1 \pm 0.3$ and slope $\gamma = 1.6 \pm 0.1$ (Paper III). We will use these estimates of $\xi(r)$ from the Durham/UKST survey in Section 6 when comparing the real and redshift space correlation functions to estimate a value of $\Omega^{0.6}/b$.

To produce a final estimate of the real and redshift space 2-point correlation functions we have combined the data from the Durham/UKST survey with that of the APM-Stromlo survey and the Las Campanas survey (Loveday et al. 1992; Loveday et al. 1995; Lin et al. 1995; Lin et al. 1996; Tucker et al. 1996). These results are shown in Fig. 7. For the redshift space 2-point correlation function (solid circles) we have combined the different data sets directly using an error weighted mean of the 3 surveys. For the real space 2-point correlation function (open circles) we use the Abel inversion method (for ease) on the 3 different $w_v(\sigma)$'s and then combine in an error weighted manner. All of the combined estimates use the weighting of Efstathiou (1988) and the estimator of Hamilton (1993). The error bars assume that each survey provides a statistically independent estimate of ξ . For comparison, we plot the real space 2-point correlation function (solid line) estimated from the inversion of the APM $w(\theta)$ by Baugh (1996).

We see that the real space $\xi(r)$ appears to quite nicely approximate a featureless single power law out to $\sim 20h^{-1}\text{Mpc}$. The high point at $\sim 30h^{-1}\text{Mpc}$ is at the end of the inversion region, where this technique becomes unreliable. This estimate agrees well with that of Baugh (1996), who also sees a slight ‘shoulder’ feature on $5 - 25h^{-1}\text{Mpc}$ scales. The redshift space $\xi(s)$ appears to have a change of shape in both amplitude and slope near $\sim 5h^{-1}\text{Mpc}$. The smaller scale effect is probably due to the velocity dispersion, which smooths the signal out, while the larger scale effect is probably due to the linear infall of galaxies, which

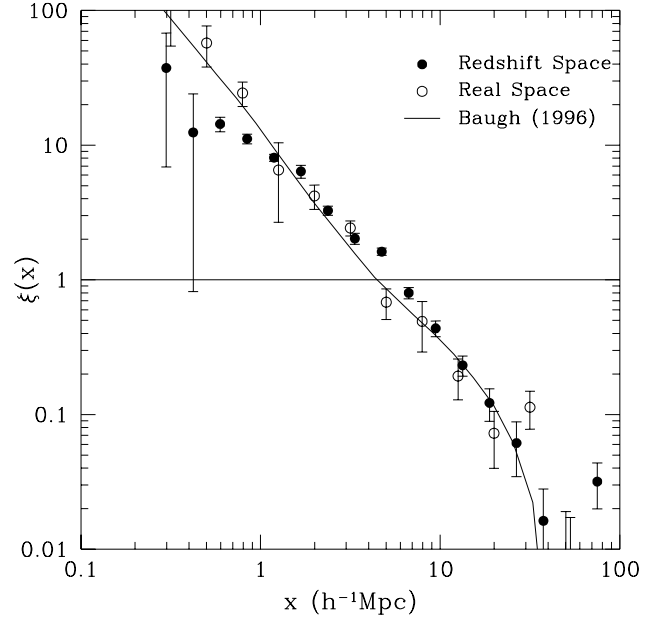


Figure 7. Comparison of the real and redshift space 2-point correlation functions obtained by combining the data from the Durham/UKST survey with that of the APM-Stromlo survey and the Las Campanas survey (Loveday et al. 1992; Loveday et al. 1995; Lin et al. 1996; Tucker et al. 1996). The solid circles show the redshift space $\xi(s)$, which is an error weighted mean of the 3 surveys. The open circles show the real space $\xi(r)$ obtained from an error weighted combination of the 3 different Abel inverted $w_v(\sigma)$'s. All of the error bars assume that each survey provides a statistically independent estimate of ξ . The solid line shows Baugh's (1996) real space $\xi(r)$ estimate which comes from the inversion of the APM $w(\theta)$.

amplifies the signal. These effects are discussed in more detail in Sections 5 and 6. Finally, we make a comment about the ‘shoulder’ feature seen in Baugh's (1996) $\xi(r)$. First evidence for such a feature was observed in $\xi(s)$ by Shanks et al. (1983) and Shanks et al. (1989) who noted the systematic increase between the amplitude of $\xi(s)$ at $r \simeq 7h^{-1}\text{Mpc}$ and the lower amplitudes obtained from $w_v(\sigma)$ at smaller scales, as continue to be found here (see Fig. 7). Some of this excess in $\xi(s)$ is now thought to be due to redshift-space distortion from infall (see Section 6) with some contribution from a real-space ‘shoulder’ in $\xi(r)$, although the evidence is stronger in the 2-D data of Baugh (1996) than in the redshift survey data presented here.

5 NON-LINEAR SCALES: THE ONE-DIMENSIONAL PAIRWISE VELOCITY DISPERSION

We now use standard modelling techniques to estimate the one-dimensional rms galaxy pairwise velocity dispersion, $\langle w^2 \rangle^{1/2}$, from the Durham/UKST survey. As we saw in Section 3 this velocity dispersion visibly elongates the $\xi(\sigma, \pi)$ contours in the line of sight direction and this is now quantitatively measured.

5.1 Modelling $\xi(\sigma, \pi)$

We follow the modelling of Peebles (1980) and define \mathbf{v} to be the peculiar velocity of a galaxy above the Hubble flow, therefore $\mathbf{w} = \mathbf{v}_i - \mathbf{v}_j$ is the peculiar velocity difference of two galaxies separated by a vector \mathbf{r} . Let $g(\mathbf{r}, \mathbf{w})$ be the distribution function of \mathbf{w} . Therefore

$$1 + \xi(\sigma, \pi) = \int [1 + \xi(r)] g(\mathbf{r}, \mathbf{w}) d^3w, \quad (15)$$

where

$$r^2 = \sigma^2 + r_z^2, \quad r_z = \pi - \frac{w_z}{H_0}, \quad (16)$$

and w_z is the component of \mathbf{w} parallel to the line of sight, which for simplicity is called the z direction. It is common to assume that g is a slowly varying function of \mathbf{r} , such that $g(\mathbf{r}, \mathbf{w}) = g(\mathbf{w})$. Therefore, one can make the approximation

$$\int dw_x \int dw_y g(\mathbf{w}) = f(w_z). \quad (17)$$

Equation 15 then becomes

$$1 + \xi(\sigma, \pi) = \int [1 + \xi(r)] f(w_z) dw_z, \quad (18)$$

which further reduces to

$$\xi(\sigma, \pi) = \int_{-\infty}^{\infty} \xi(r) f(w_z) dw_z, \quad (19)$$

when the unit normalisation of $f(w_z)$ is considered. A streaming model which describes the relative bulk motion of galaxies towards (or away from) each other can be incorporated as follows

$$g(\mathbf{r}, \mathbf{w}) = g(\mathbf{w} - \hat{\mathbf{r}}v(r)), \quad (20)$$

where $v(r)$ is the streaming model in question. Equation 15 then becomes

$$1 + \xi(\sigma, \pi) = \int [1 + \xi(r)] f(w_z - v(r_z)) dw_z, \quad (21)$$

$$= \int_{-\infty}^{\infty} \left[1 + \xi \left(\sqrt{\sigma^2 + r_z^2} \right) \right] f[w_z - v(r_z)] dw_z. \quad (22)$$

Obviously, we require models for the real space 2-point correlation function, $\xi(r)$, the distribution function, $f(w_z)$, and the streaming motion, $v(r_z)$. The real space 2-point correlation function is simply modelled by a power law, $\xi(r) = (r_0/r)^\gamma$, which should be accurate out to $\sim 20h^{-1}$ Mpc. For the distribution function we tried both exponential and Gaussian functions and found that the exponential provided a significantly better fit to the shape of the N -body simulation results and so is used exclusively here

$$f(w_z) = \frac{1}{\sqrt{2} \langle w^2 \rangle^{1/2}} \exp \left[-\sqrt{2} \frac{|w_z|}{\langle w^2 \rangle^{1/2}} \right], \quad (23)$$

where $\langle w^2 \rangle^{1/2}$ is the rms pairwise velocity dispersion, namely the second moment of the distribution function $f(w_z)$

$$\langle w^2 \rangle = \int_{-\infty}^{\infty} f(w_z) w_z^2 dw_z. \quad (24)$$

A realistic streaming model might be expected to depend on the clustering, biasing and mean mass density of the

universe. The infall model of Bean et al. (1983) takes the maximal approach by assuming $\Omega = 1$, $b = 1$ and uses the second BBGKY equation (e.g. Peebles 1980) to give

$$v(r_z) = -H_0 r_z \left[\frac{\xi(r_z)}{1 + \xi(r_z)} \right]. \quad (25)$$

We favour this streaming model in the analysis presented here.

5.2 Testing the Modelling

We have tested this modelling with both the CDM simulations and mock catalogues. Before describing these tests we first present the answers we are trying to reproduce. We have calculated the values of $\langle w^2 \rangle^{1/2}$ directly from the simulations and find that $\langle w^2 \rangle^{1/2} \simeq 950$ and 750 kms^{-1} on $\sim 1h^{-1}$ Mpc scales for the SCDM and LCDM models, respectively. In Paper II we estimated the real space $\xi(r)$ correlation lengths to be $\sim 5.0h^{-1}$ Mpc and $\sim 6.0h^{-1}$ Mpc for the SCDM and LCDM models, respectively. For both of these models the slope of the real space $\xi(r)$ was ~ 2.2 .

In the fitting procedure there are three parameters which can be estimated, $\langle w^2 \rangle^{1/2}$, r_0 and γ . Given our available computing constraints we only choose to fit for two of these and fix γ to be a constant value. The results obtained from this procedure are insensitive to the value of γ chosen, provided a realistic value is used. For the CDM simulations we use $\gamma = 2.2$. Also, when the streaming model is used we assume that $r_0 = 5.0\text{--}6.0h^{-1}$ Mpc in equation 25 only, again the fits are relatively insensitive to the value chosen. We fit $\langle w^2 \rangle^{1/2}$ and r_0 using an approximate χ^2 statistic in the range $0\text{--}20h^{-1}$ Mpc for four different values of σ , with the standard deviations from the simulations or mock catalogues being used accordingly in the χ^2 statistic. The results of these fits using the $\xi(\sigma, \pi)$ estimated directly from the N -body simulations are shown in Figs. 8 and 9 for the SCDM and LCDM models, respectively, with the best fit values given in Table 1. The solid histogram denotes the averaged $\xi(\sigma, \pi)$ in the quoted σ range, while the solid and dotted lines show the fits with and without the streaming model, respectively. Similarly, Table 2 shows the results of the fits to the optimally estimated $\xi(\sigma, \pi)$ from the SCDM and LCDM mock catalogues. The quoted error bars on the mock catalogue results come from the 1σ standard deviation between the mock catalogues and therefore reflects the error on an individual mock catalogue.

The results from the CDM simulations show that the streaming model only becomes important (in terms of producing consistent results for $\langle w^2 \rangle^{1/2}$) when $\sigma > 1\text{--}2h^{-1}$ Mpc. Of course, this assumes that $\langle w^2 \rangle^{1/2}$ does not vary with σ . The best fit values to the CDM simulation results (with streaming), had $\langle w^2 \rangle^{1/2} = 980 \pm 22 \text{ kms}^{-1}$, $r_0 = 5.00 \pm 0.24h^{-1}$ Mpc for the SCDM model and $\langle w^2 \rangle^{1/2} = 835 \pm 60 \text{ kms}^{-1}$, $r_0 = 5.12 \pm 0.69h^{-1}$ Mpc for the LCDM model. These quoted errors simply come from the scatter in the best fit values of Table 1. The values of $\langle w^2 \rangle^{1/2}$ can be compared with those estimated directly from the N -body simulations on $\sim 1h^{-1}$ Mpc scales, namely 950 and 750 kms^{-1} for the SCDM and LCDM models, respectively. This agreement is adequate given the slightly ad hoc assumption of an exponential distribution function.

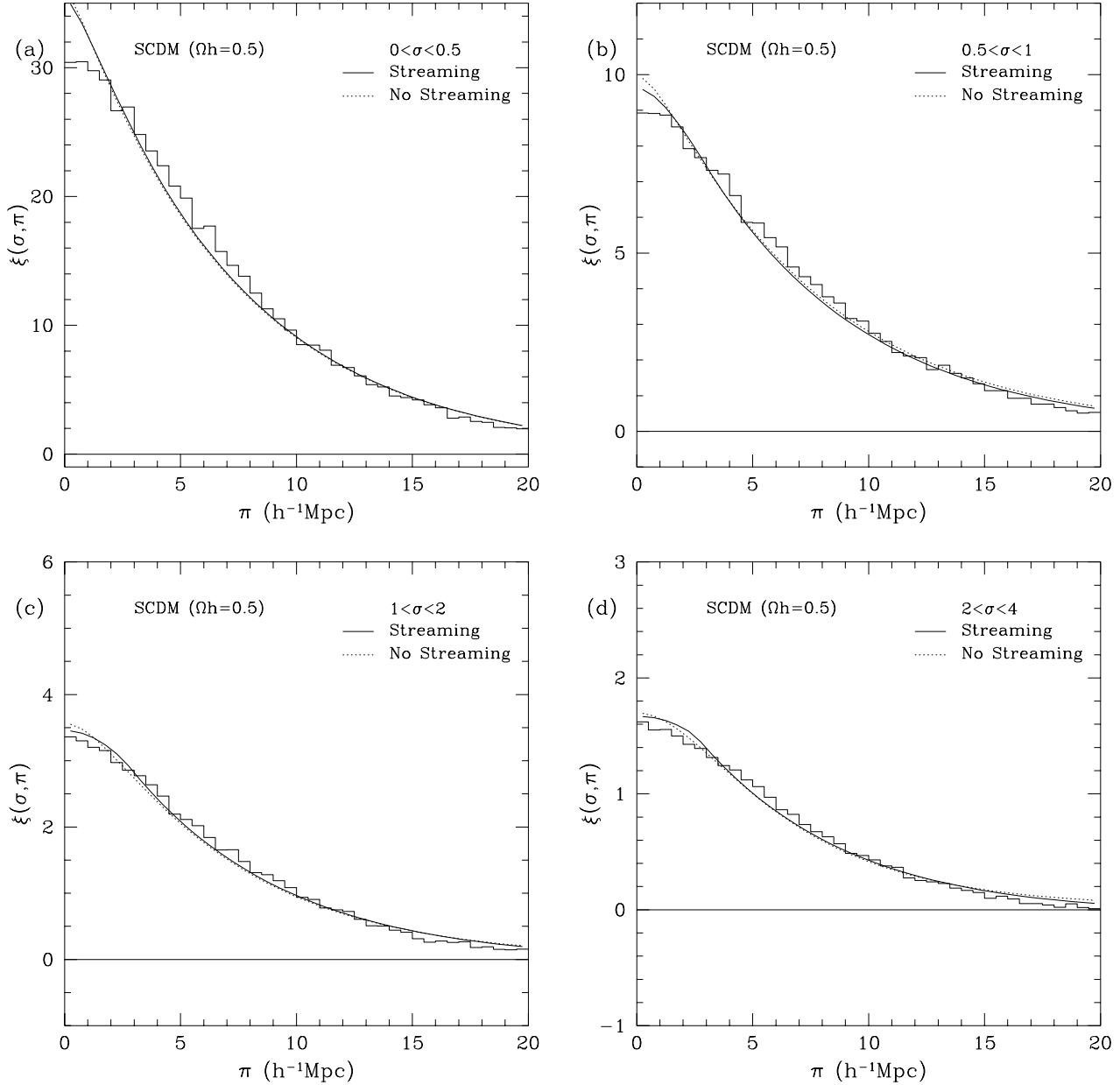


Figure 8. Histograms of $\xi(\sigma, \pi)$ estimated from the SCDM N -body simulations as a function of π for different (constant) values of σ . The solid curve shows the minimum χ^2 fit using the modelling of Section 5.1 with a streaming model, while the dotted curve shows the fit without the streaming model.

The values of r_0 can be compared with the approximate real space values estimated in Paper III, namely $5.0h^{-1}\text{Mpc}$ and $6.0h^{-1}\text{Mpc}$ for the SCDM and LCDM models, respectively. Again, the agreement is adequate in both cases although slightly small for the LCDM model. However, closer inspection of the LCDM $\xi(r)$ plot on $r \leq 1h^{-1}\text{Mpc}$ scales shows that r_0 is slightly lower in this region, $\sim 5.0h^{-1}\text{Mpc}$, which probably explains our measurement.

The results from the CDM mock catalogues confirm the conclusions drawn from the CDM simulation results. All of the $\langle w^2 \rangle^{1/2}$ values in Table 2 agree well with their counterparts in Table 1 given the quoted errors (on an individual

mock catalogue). A similar statement can be made for the values of r_0 estimated from these mock catalogues.

Overall, our tests confirm that the correct $\langle w^2 \rangle^{1/2}$ and r_0 can be reproduced by this method which models the elongation in $\xi(\sigma, \pi)$. This holds for both the $\xi(\sigma, \pi)$ estimated directly from the N -body simulations and that estimated using the optimal techniques for ξ from the mock catalogues, albeit with larger scatter in this case.

5.3 Results from the Durham/UKST Survey

We now apply the modelling of Section 5.1 to the Durham/UKST survey. We use the optimally estimated

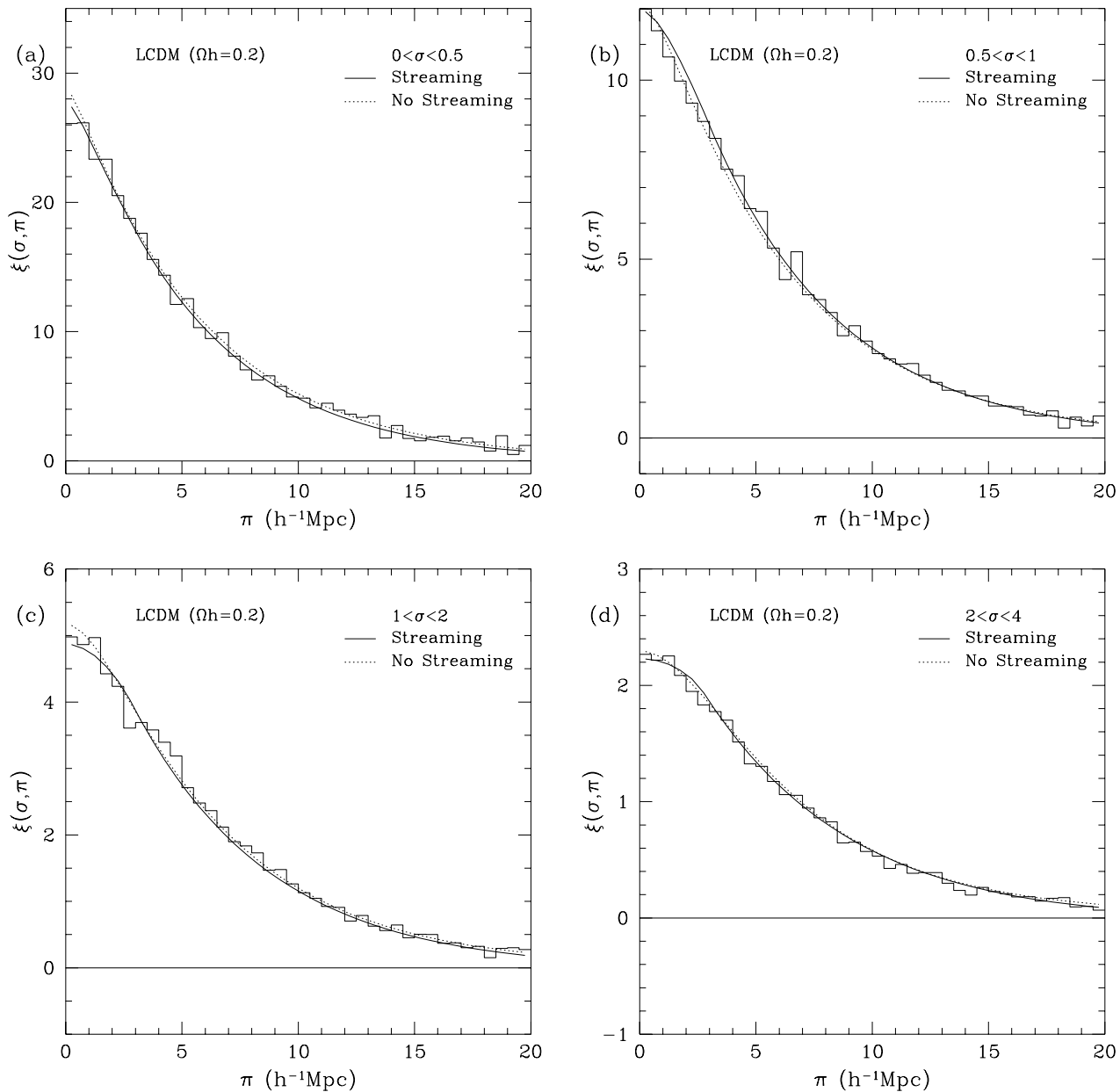


Figure 9. Histograms of $\xi(\sigma, \pi)$ estimated from the LCDM N -body simulations as a function of π for different (constant) values of σ . The solid curve shows the minimum χ^2 fit using the modelling of Section 5.1 with a streaming model, while the dotted curve shows the fit without the streaming model.

$\xi(\sigma, \pi)$ data which was shown in Fig. 2 and described in Section 3.3. Fig. 10 shows the histograms of $\xi(\sigma, \pi)$ as a function of π for different (constant) values of σ . The solid curve shows the minimum χ^2 fit of the model from Section 5.1 with the streaming model. The dotted curve shows the same fit without the streaming model. The results of these fits are given in Table 3 where we have assumed $\gamma = 1.7$. Small changes in this value of γ do not significantly affect our results. We use the standard deviations on an individual LCDM mock catalogue in the χ^2 fits. These fits are more than likely biased low by the non-independent nature of the points. The errors on the parameters quoted in Table 3 come from the appropriate $\Delta\chi^2$ contour about the minimum.

We can make a few comments about these results. Firstly, the streaming model is again required to produce consistent fits for $\langle w^2 \rangle^{1/2}$ for $\sigma > 1-2h^{-1}\text{Mpc}$ (assuming that it does not change with σ). Secondly, although not shown we also fitted for a Gaussian distribution function (rather than the exponential one favoured by the simulations) and found that the noise in the data implied a similar quality of fit for both forms. Therefore, this data did not allow one to distinguish between the two models. Finally, we combine the results for the exponential velocity distribution function with the streaming model at each σ value to produce an overall estimate of $\langle w^2 \rangle^{1/2}$ and r_0 . Assuming that each quoted estimate is independent gives

Table 1. Minimum χ^2 fits for $\langle w^2 \rangle^{1/2}$ and r_0 from the CDM N -body simulations using the exponential distribution function with and without the streaming model.

σ ($h^{-1}\text{Mpc}$)	$\langle w^2 \rangle^{1/2}$ (kms^{-1})	r_0 ($h^{-1}\text{Mpc}$)	χ^2 ($N_{bin} = 40$)
SCDM			
Streaming Model			
[0, 0.5]	990	5.1	40.0
[0.5, 1]	1000	5.3	24.7
[1, 2]	980	4.8	21.2
[2, 4]	950	4.8	34.4
No Streaming Model			
[0, 0.5]	970	5.1	46.3
[0.5, 1]	960	5.4	32.3
[1, 2]	800	4.9	28.7
[2, 4]	550	5.1	48.2
LCDM			
Streaming Model			
[0, 0.5]	770	4.1	13.8
[0.5, 1]	810	5.3	7.8
[1, 2]	850	5.4	16.5
[2, 4]	910	5.6	11.1
No Streaming Model			
[0, 0.5]	780	4.2	14.2
[0.5, 1]	760	5.4	8.1
[1, 2]	720	5.6	14.0
[2, 4]	570	5.9	9.0

Table 2. Minimum χ^2 fits for $\langle w^2 \rangle^{1/2}$ and r_0 from the CDM mock catalogues using the exponential distribution function with and without the streaming model.

σ ($h^{-1}\text{Mpc}$)	$\langle w^2 \rangle^{1/2}$ (kms^{-1})	r_0 ($h^{-1}\text{Mpc}$)
SCDM		
Streaming Model		
[0, 0.5]	930 ± 190	5.0 ± 0.4
[0.5, 1]	970 ± 180	5.3 ± 0.4
[1, 2]	920 ± 260	4.6 ± 0.5
[2, 4]	810 ± 180	4.5 ± 0.6
No Streaming Model		
[0, 0.5]	920 ± 190	5.0 ± 0.4
[0.5, 1]	910 ± 170	5.3 ± 0.4
[1, 2]	750 ± 230	4.8 ± 0.4
[2, 4]	450 ± 130	5.0 ± 0.4
LCDM		
Streaming Model		
[0, 0.5]	610 ± 180	3.8 ± 0.3
[0.5, 1]	790 ± 230	5.2 ± 0.7
[1, 2]	840 ± 130	5.2 ± 0.7
[2, 4]	780 ± 150	5.2 ± 0.7
No Streaming Model		
[0, 0.5]	590 ± 170	3.9 ± 0.3
[0.5, 1]	750 ± 220	5.2 ± 0.6
[1, 2]	690 ± 130	5.3 ± 0.7
[2, 4]	440 ± 140	5.6 ± 0.6

Table 3. Minimum χ^2 fits for $\langle w^2 \rangle^{1/2}$ and r_0 from the Durham/UKST survey using the exponential distribution function with and without the streaming model.

σ ($h^{-1}\text{Mpc}$)	$\langle w^2 \rangle^{1/2}$ (kms^{-1})	r_0 ($h^{-1}\text{Mpc}$)	χ^2 ($N_{bin} = 40$)
Durham/UKST			
Streaming Model			
[0, 0.5]	510 ± 120	5.1 ± 0.6	19.0
[0.5, 1]	300 ± 50	4.7 ± 0.3	23.5
[1, 2]	500 ± 65	4.5 ± 0.2	29.6
[2, 4]	500 ± 65	4.7 ± 0.4	48.0
No Streaming Model			
[0, 0.5]	470 ± 130	5.2 ± 0.6	19.1
[0.5, 1]	180 ± 70	4.8 ± 0.4	24.0
[1, 2]	270 ± 90	4.8 ± 0.3	29.5
[2, 4]	180 ± 80	5.5 ± 0.2	56.1

$\langle w^2 \rangle^{1/2} = 416 \pm 36 \text{ kms}^{-1}$, $r_0 = 4.6 \pm 0.2 h^{-1}\text{Mpc}$. We make the comment that this value of r_0 agrees well with those estimated from the Durham/UKST survey using other methods, see Section 4.4. These results are discussed in more detail in Section 7 where comparisons with the results from structure formation models and other redshift surveys are made.

6 LINEAR SCALES: INFALL AND $\Omega^{0.6}/B$

We now use modelling techniques developed from the linear theory result of Kaiser (1987) to estimate the quantity $\Omega^{0.6}/b$ from the Durham/UKST survey. We saw in Section 3 that on non-linear scales the velocity dispersion was mainly responsible for the anisotropies in $\xi(\sigma, \pi)$. However, in Section 5 we saw that to produce consistent results it was also necessary to incorporate a model which imitated the streaming motions of galaxies. It is this infall of galaxies into over-dense regions that visibly distorts the $\xi(\sigma, \pi)$ contours on larger scales and this compression in the line of sight direction is now quantitatively measured.

6.1 Modelling $\xi(\sigma, \pi)$

Kaiser (1987) used the distant observer approximation in the linear regime of gravitational instability to show that the strength of an individual plane wave as measured in redshift space is amplified over that measured in real space by a factor

$$\delta_{\mathbf{k}}^s = \delta_{\mathbf{k}}^r (1 + \mu_{\mathbf{k}\mathbf{l}}^2 f(\Omega)/b), \quad (26)$$

where $\delta_{\mathbf{k}}^r$ and $\delta_{\mathbf{k}}^s$ are the Fourier amplitudes in real (r) and redshift (s) space, respectively, $\mu_{\mathbf{k}\mathbf{l}}$ is the cosine of the angle between the wavevector (\mathbf{k}) and the line of sight (\mathbf{l}), $f(\Omega) \simeq \Omega^{0.6}$ is the logarithmic derivative of the fluctuation growth rate (e.g. Peebles 1980) and b is the linear bias factor relating the galaxy and mass distributions, $(\Delta\rho/\rho)_g = b(\Delta\rho/\rho)_m$. The distant observer approximation restricts use of equation 26 to opening angles in a redshift survey of less than $\sim 50^\circ$ which can cause a systematic effect at the $\sim 5\%$ level in $f(\Omega)/b$ (Cole, Fisher & Weinberg 1994).

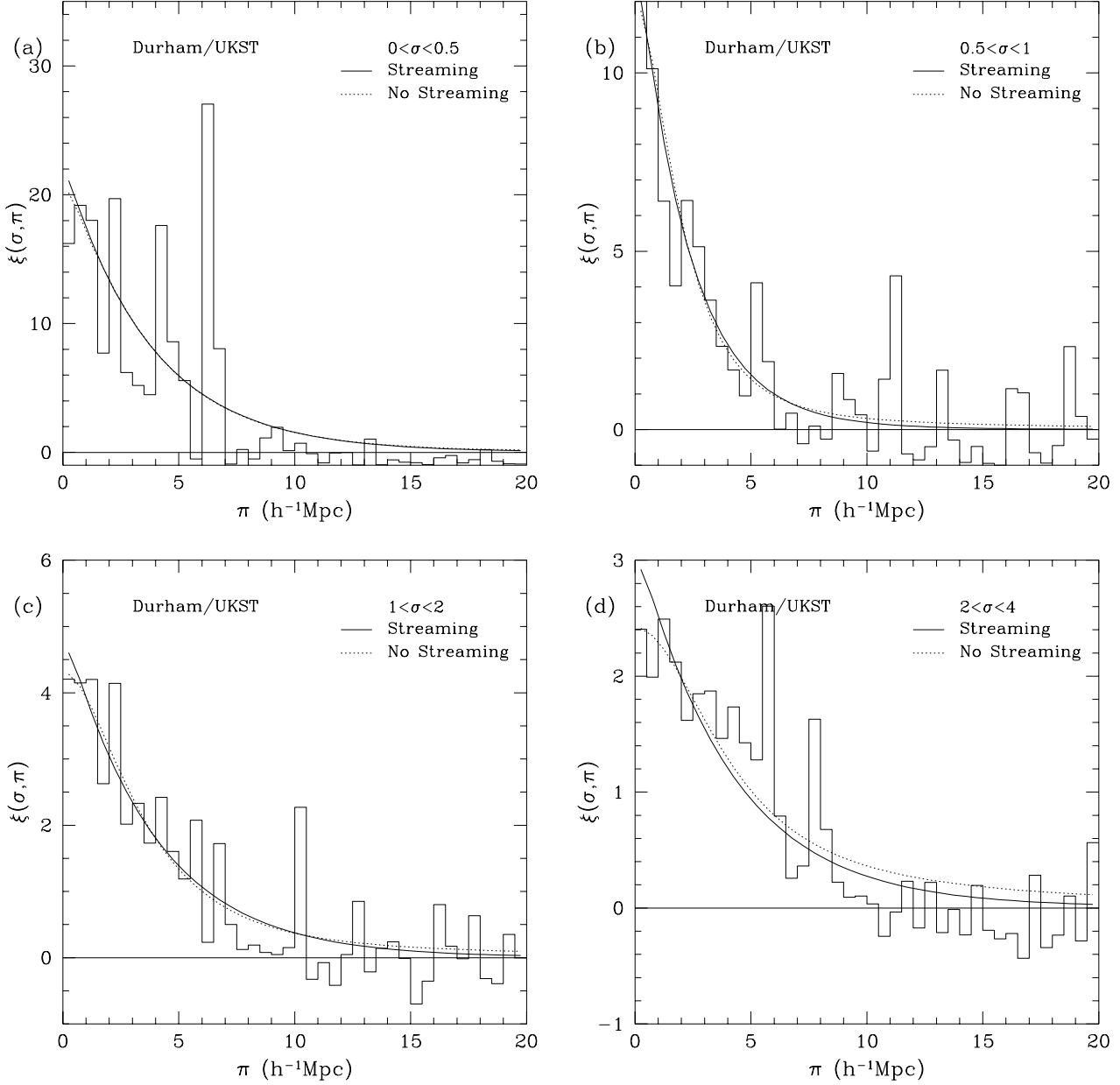


Figure 10. Histograms of $\xi(\sigma, \pi)$ estimated from the Durham/UKST survey as a function of π for different (constant) values of σ . The solid curve shows the minimum χ^2 fit using the modelling of Section 5.1 with a streaming model, while the dotted curve shows the fit without the streaming model.

This $(1 + \mu_{\mathbf{k}\mathbf{l}}^2 f(\Omega)/b)$ factor propagates directly through to the power spectrum, $P(k, \mu_{\mathbf{k}\mathbf{l}}) \equiv \langle \delta_{\mathbf{k}} \delta_{\mathbf{l}}^* \rangle$

$$P^s(k, \mu_{\mathbf{k}\mathbf{l}}) = P^r(k) \left(1 + \mu_{\mathbf{k}\mathbf{l}}^2 f(\Omega)/b\right)^2, \quad (27)$$

where the real space $P^r(k)$ is assumed to be an isotropic function of k only. Thus the anisotropy is a strong function of the angle between \mathbf{k} and \mathbf{l} . Integrating over all $\mu_{\mathbf{k}\mathbf{l}}$ gives the angle-averaged redshift space $P^s(k)$

$$P^s(k) = \frac{\int_{-1}^1 d\mu_{\mathbf{k}\mathbf{l}} P^s(k, \mu_{\mathbf{k}\mathbf{l}})}{\int_{-1}^1 d\mu_{\mathbf{k}\mathbf{l}}}, \quad (28)$$

$$= P^r(k) \left[1 + \frac{2}{3} \frac{f(\Omega)}{b} + \frac{1}{5} \left(\frac{f(\Omega)}{b} \right)^2 \right]. \quad (29)$$

Fourier transforming equation 29 (which has no explicit $\mu_{\mathbf{k}\mathbf{l}}$ dependence) gives the corresponding relation between the angle-averaged $\xi(s)$ and $\xi(r)$

$$\xi(s) = \xi(r) \left[1 + \frac{2}{3} \frac{f(\Omega)}{b} + \frac{1}{5} \left(\frac{f(\Omega)}{b} \right)^2 \right], \quad (30)$$

assuming that $\xi(r)$ is an isotropic function of r only. If the volume integral of ξ is defined as

$$J_3(x) = \int_0^x \xi(y)y^2 dy, \quad (31)$$

then

$$J_3(s) = J_3(r) \left[1 + \frac{2}{3} \frac{f(\Omega)}{b} + \frac{1}{5} \left(\frac{f(\Omega)}{b} \right)^2 \right]. \quad (32)$$

We will use equations 30 and 32 as two of our methods for estimating $\Omega^{0.6}/b$.

Hamilton (1992) has extended Kaiser's (1987) analysis by Fourier transforming equation 27 and noting that the cosine factor in Fourier space, $\mu_{\mathbf{k}\mathbf{l}}^2 \equiv k_1^2/k^2$, becomes a differential operator in real space, $(\partial/\partial|\mathbf{l}|)^2(\nabla^2)^{-1}$. Therefore equation 27 becomes

$$\xi^s(r, \mu_{\mathbf{r}\mathbf{l}}) = \left(1 + (f(\Omega)/b)(\partial/\partial|\mathbf{l}|)^2(\nabla^2)^{-1} \right)^2 \xi^r(r), \quad (33)$$

where $\mu_{\mathbf{r}\mathbf{l}}$ is the cosine of the angle between the pair separation, \mathbf{r} , and the line of sight, \mathbf{l} . Hamilton (1992) then shows that the solution of this equation can be written in terms of the first three even spherical harmonics of $\xi^s(r, \mu_{\mathbf{r}\mathbf{l}})$, with the higher moments zero (and all odd moments zero by definition)

$$\xi^s(r, \mu_{\mathbf{r}\mathbf{l}}) = \xi_0(r)P_0(\mu_{\mathbf{r}\mathbf{l}}) + \xi_2(r)P_2(\mu_{\mathbf{r}\mathbf{l}}) + \xi_4(r)P_4(\mu_{\mathbf{r}\mathbf{l}}), \quad (34)$$

where $P_l(\mu_{\mathbf{r}\mathbf{l}})$ are the usual Legendre polynomials and

$$\xi_l(r) = \frac{2l+1}{2} \int_{-1}^1 \xi^s(r, \mu_{\mathbf{r}\mathbf{l}}) P_l(\mu_{\mathbf{r}\mathbf{l}}) d\mu_{\mathbf{r}\mathbf{l}}. \quad (35)$$

Arguably the most useful form of Hamilton's (1992) solution is that expressed in terms of ξ_0 and ξ_2 only

$$\left[1 + \frac{2}{3} \frac{f(\Omega)}{b} + \frac{1}{5} \left(\frac{f(\Omega)}{b} \right)^2 \right] \xi_2(r) = \left[\frac{4}{3} \frac{f(\Omega)}{b} + \frac{4}{7} \left(\frac{f(\Omega)}{b} \right)^2 \right] \left(\xi_0(r) - \frac{3}{r^3} \int_0^r \xi_0(s)s^2 ds \right),$$

or by defining

$$\tilde{\xi}_0(r) = -\xi_0(r) + \frac{3}{r^3} \int_0^r \xi_0(s)s^2 ds, \quad (36)$$

$$\tilde{\xi}_2(r) = -\xi_2(r), \quad (37)$$

it can be written as

$$\frac{\tilde{\xi}_2}{\tilde{\xi}_0} = \frac{\left(\frac{4}{3}\beta + \frac{4}{7}\beta^2 \right)}{\left(1 + \frac{2}{3}\beta + \frac{1}{5}\beta^2 \right)}. \quad (38)$$

We will use the ratio in equation 38 as our third method for estimating $\Omega^{0.6}/b$.

6.2 Testing the Modelling

We have tested this modelling with the LCDM simulations and mock catalogues. The SCDM model was not analysed because we felt that the one-dimensional rms galaxy pairwise velocity dispersion too strongly dominated the $\xi(\sigma, \pi)$ plots for a sensible answer to be obtained. As will be shown below this is also the case for some aspects of the LCDM model. Also, in Section 6.1 we noted that equation 26 and the subsequent analysis is only strictly correct in the distant observer approximation and that data from redshift survey opening angles of $\leq 50^\circ$ should only really be used. For redshift surveys geometrically similar to the Durham/UKST

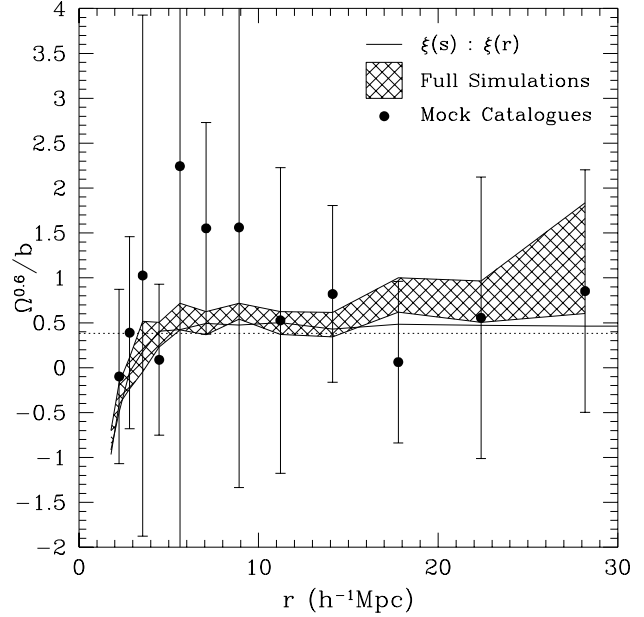


Figure 11. Estimates of $\Omega^{0.6}/b$ obtained from the LCDM model using the method involving the ratio of real to redshift space 2-point correlation functions (equation 30). The solid line denotes the results obtained by averaging the ξ 's from each N -body simulation and then manipulating to get an estimate of $\Omega^{0.6}/b$. The shaded area denotes the 68% confidence region in $\Omega^{0.6}/b$ obtained from the scatter seen between the N -body simulation ξ results. The solid points denote the mean of the results obtained from the mock catalogues. The error bars on these points are the observed standard deviation on an individual mock catalogue.

survey this restriction has a negligible impact on the analysis techniques.

In Figs. 11, 12 and 13 the following conventions are adopted: the dotted line denotes the expected value of $f(\Omega)/b \simeq \Omega^{0.6}/b = (0.2)^{0.6}/1 \simeq 0.38$; the solid line denotes the result for $\Omega^{0.6}/b$ obtained from the average of the LCDM simulations (i.e. estimate an averaged $\xi(\sigma, \pi)$ from the 5 simulations and then manipulate to get one value of $\Omega^{0.6}/b$); the shaded area denotes the 68% confidence region in $\Omega^{0.6}/b$ obtained from the scatter seen between the LCDM simulations (i.e. take the $\xi(\sigma, \pi)$ from each of the 5 simulations, manipulate to get 5 values of $\Omega^{0.6}/b$ and then average at the end); and the points with error bars are the mean and 1σ scatter seen in the LCDM mock catalogues (i.e. take the $\xi(\sigma, \pi)$ from each of the 15 mock catalogues, manipulate to get 15 values of $\Omega^{0.6}/b$ and then average at the end). These errors are the observed standard deviation between the mock catalogues and therefore reflect the error on an individual mock catalogue.

The results from equation 30 are shown in Fig. 11. This method uses the ratio of the real to redshift space ξ 's to estimate $\Omega^{0.6}/b$. We estimate $\xi(s)$ using the methods described in Paper III. We estimate $\xi(r)$ using the Abel inversion of the projected correlation function, $w_v(\sigma)$, with a $\pi_{cut} = 30h^{-1}\text{Mpc}$, as described in Section 4. Examining the results obtained from the averaged ξ of the simulations (solid line), it appears that the method itself is not dominated by non-linear effects above $\sim 6h^{-1}\text{Mpc}$, although they

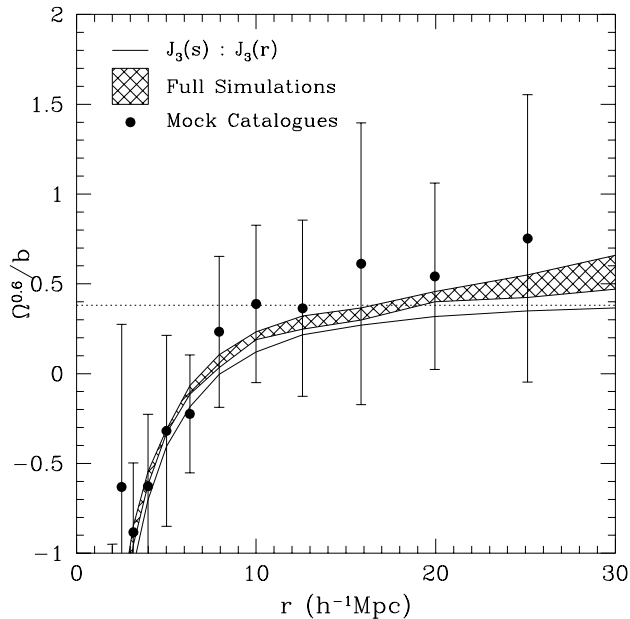


Figure 12. The same as Fig. 11 but the $\Omega^{0.6}/b$ results use the method involving the ratio of real to redshift space volume integrated 2-point correlation functions (equation 32).

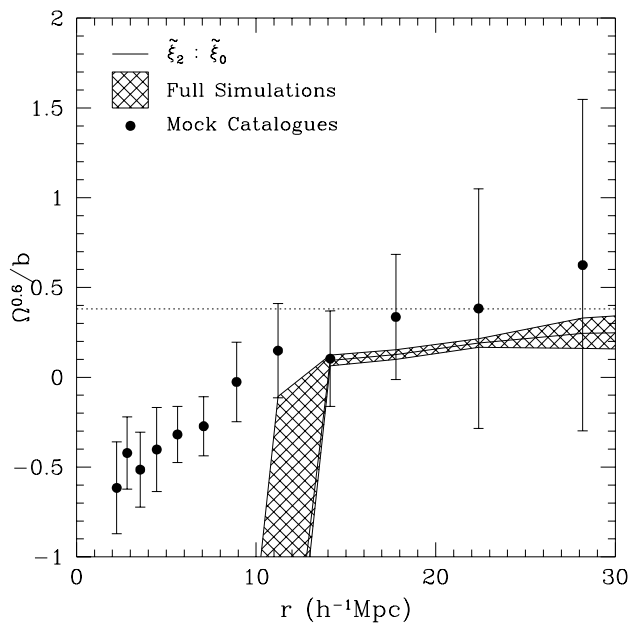


Figure 13. The same as Fig. 11 but the $\Omega^{0.6}/b$ results use the method involving a ratio incorporating the second and zeroth spherical harmonics of the redshift space 2-point correlation function (equation 38).

could cause the ~ 0.1 systematic offset in $\Omega^{0.6}/b$ that is seen out to $> 30h^{-1}\text{Mpc}$. Unfortunately, the results obtained by averaging the 5 estimates of $\Omega^{0.6}/b$ from each (full) simulation show that noise begins to dominate the inversion process between $15\text{--}20h^{-1}\text{Mpc}$. For the mock catalogues noise dominates at all scales and the results resemble a scatter plot in places. Overall, this method appears relatively in-

sensitive to non-linear effects but the large scatter (for the mock catalogues) renders the method almost useless in this case.

The results from equation 32 are shown in Fig. 12. This method uses the ratio of the real to redshift space J_3 's to estimate $\Omega^{0.6}/b$. We estimate $J_3(s)$ by evaluating the integral in equation 31 using the above $\xi(s)$. We estimate $J_3(r)$ from the same integral but using the above $\xi(r)$. Examining the results obtained from the averaged ξ of the simulations, it appears that the method itself is not dominated by non-linear effects above $\sim 15h^{-1}\text{Mpc}$. The results obtained by averaging the 5 estimates of $\Omega^{0.6}/b$ from each simulation are similarly consistent with the expected value. The results obtained from the mock catalogues also reproduce the correct answer but with a larger scatter. Overall, this method is considerably more successful (in terms of more accurate results) than the $\xi(s)/\xi(r)$ one. However, one does pay a price by having to go to larger scales before the non-linearities become negligible and the integration procedure also makes the points highly correlated.

The results from equation 38 are shown in Fig. 13. This method uses the ratio involving the second and zeroth spherical harmonics of ξ to estimate $\Omega^{0.6}/b$. The ξ_l 's are estimated using equation 35, which in practice becomes

$$\xi_l(r) = (2l + 1)\Delta\mu_{r1} \sum_i^{\mu_{r1}^i > 0} \xi^s(r, \mu_{r1}^i) P_l(\mu_{r1}^i), \quad (39)$$

and we use a binning of $\Delta\mu_{r1} = 0.2$. Examining the results obtained from the averaged ξ of the simulations, it appears that the method itself is severely affected by non-linearities which cause a negative value of $\Omega^{0.6}/b$ to be measured until $\sim 13h^{-1}\text{Mpc}$. (Such a negative value is obviously unphysical and simply due to the shape of the $\xi(\sigma, \pi)$ contours.) Similar results are found by averaging the 5 estimates of $\Omega^{0.6}/b$ from each simulation. The results obtained from the mock catalogues trace the simulation results adequately, although not on scales $< 10h^{-1}\text{Mpc}$ where they appear biased high. Overall, the impression is that the non-linearities make this method redundant. However, when considering the Durham/UKST survey one must remember that its value of the velocity dispersion is almost half that of the LCDM model. Therefore, the elongation in $\xi(\sigma, \pi)$ which causes the above problems will be significantly lower.

6.3 Results from the Durham/UKST Survey

We now apply the modelling of Section 6.1 to the Durham/UKST survey. We calculate our results using the optimally estimated 2-point correlation function described in Section 3.3 and Paper III. Before presenting our results of $\Omega^{0.6}/b$ we show the data which produced them. Fig. 14 shows the real and redshift space ξ 's, where $\xi(s)$ is estimated directly from the redshift survey and $\xi(r)$ comes from the Abel inversion of Section 4.2 shown in Fig. 4. Fig. 15 shows the real and redshift space J_3 's, where the integral in equation 31 is applied to the above ξ 's. Fig. 16 shows the zeroth and second spherical harmonics estimated using equation 39 on the optimally estimated $\xi^s(r, \mu_{r1})$. The error bars shown are those estimated from the scatter between the 4 quadrants of the Durham/UKST survey. These errors were of a

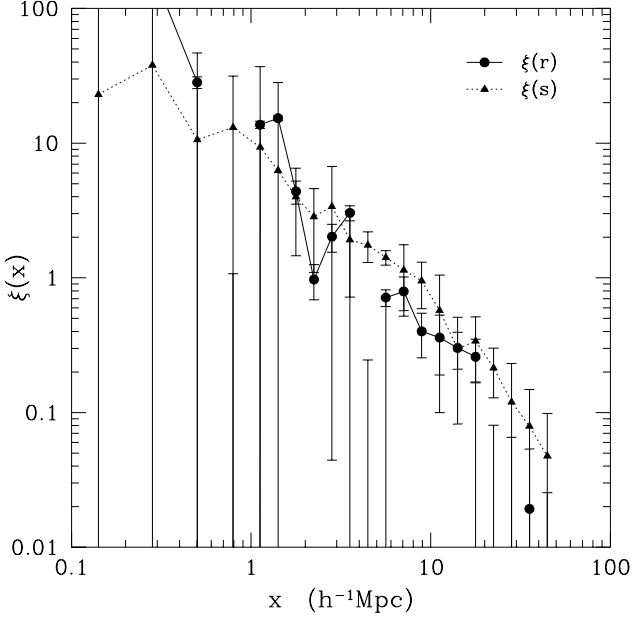


Figure 14. Comparison of the real and redshift space 2-point correlation functions optimally estimated from the Durham/UKST survey. $\xi(s)$ was estimated directly from the redshift survey (solid triangles connected by the dotted line) and $\xi(r)$ comes from the Abel inversion of Section 4.2 shown in Fig. 4 (solid circles connected by the solid line). The error bars denote the scatter seen between in the 4 quadrants of the Durham/UKST survey.

very similar size to those estimated on an individual LCDM mock catalogue.

We comment briefly on the results in each of these figures. Firstly, Fig. 14 shows that $\xi(r) > \xi(s)$ below $\sim 1h^{-1}\text{Mpc}$, while $\xi(s) > \xi(r)$ on larger scales. This was described in Section 4.4. Unfortunately, the noise in these estimates is very high and it will more than likely make any measurement of $\Omega^{0.6}/b$ redundant. Secondly, Fig. 15 shows that, once again, at small separations $J_3(r) > J_3(s)$, while at larger separations $J_3(s) > J_3(r)$. There appears to be a near constant offset in the real/redshift $\lg J_3$'s on scales $10\text{--}20h^{-1}\text{Mpc}$ (i.e. a constant multiplicative factor in linear J_3). This should give a consistent estimate of $\Omega^{0.6}/b$ on these scales. Finally, Fig. 16 shows that ξ_2 is positive until $\sim 8h^{-1}\text{Mpc}$, which is caused by the elongation of the $\xi(\sigma, \pi)$ contours parallel to the line of sight. On larger separations ξ_2 is negative due to the compression of the $\xi(\sigma, \pi)$ contours parallel to the line of sight. Therefore, there appears to be a significant signal to measure in this method.

We now present the results for $\Omega^{0.6}/b$ estimated from the Durham/UKST survey. Fig. 17 shows the results of applying equation 30 (solid squares), equation 32 (solid triangles) and equation 38 (solid circles) to the data in Figs. 14, 15 and 16, respectively. The plotted errors denote the standard deviation seen between the 4 quadrants of the Durham/UKST survey. Similarly sized errors were seen in the scatter between the individual LCDM mock catalogues. For clarity, error bars are not shown for the $\xi(s)/\xi(r)$ method because they are very large and only cause confusion.

We can make a few comments about the results from

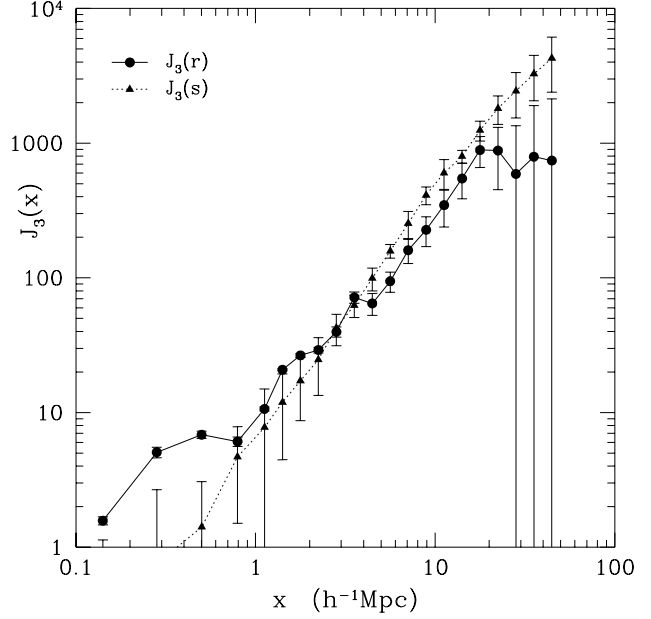


Figure 15. Comparison of the real and redshift space J_3 's estimated from the Durham/UKST survey. These were calculated using the integral in equation 31 with the ξ 's of Fig. 14. Again, the error bars denote the scatter seen between in the 4 quadrants of the Durham/UKST survey.

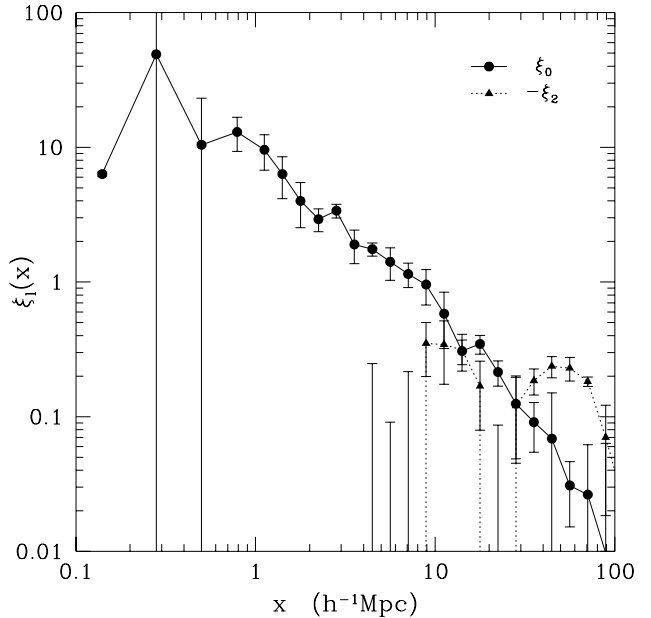


Figure 16. The zeroth and second spherical harmonics from the Durham/UKST survey. These were calculated using equation 39 on the optimally estimated $\xi^s(r, \mu_{r1})$. The solid circles connected by the solid line shows ξ_0 , while the solid triangles connected by the dotted line shows $-\xi_2$. Note that $-\xi_2$ is plotted so that it is positive in the large scale region of interest. Again, the error bars denote the scatter seen between in the 4 quadrants of the Durham/UKST survey.

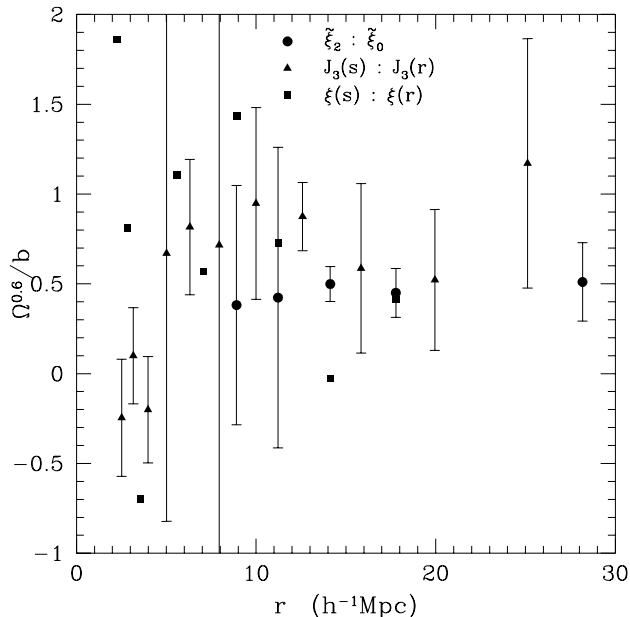


Figure 17. Estimates of $\Omega^{0.6}/b$ obtained from the Durham/UKST survey. We use the three methods from equation 30 (solid squares), equation 32 (solid triangles) and equation 38 (solid circles) and apply them to the data in Figs. 14, 15 and 16, respectively. The plotted errors denote the standard deviation seen between the 4 quadrants of the Durham/UKST survey. For clarity, error bars are not shown for the $\xi(s)/\xi(r)$ method because they are very large and only cause confusion.

these three methods. Section 6.2 showed that our region of interest is $\sim 10\text{--}30h^{-1}\text{Mpc}$ because of non-linear effects on smaller scales and noise on larger scales. For the $\xi(s)/\xi(r)$ method, the points have no systematic trend (other than a large random scatter) and we discount them from the further analysis. For the $J_3(s)/J_3(r)$ method, we obtain quite consistent results although one must remember that these points are not independent because of the integration procedure. We choose to quote the value at $\sim 20h^{-1}\text{Mpc}$ as being representative of our results, $\Omega^{0.6}/b = 0.52 \pm 0.39$. We believe that we are being very conservative with this quoted error and, for example, the point at $\sim 12h^{-1}\text{Mpc}$ only has an error of ± 0.19 . For the ξ_2/ξ_0 method, we again obtain very consistent results and quote the value at $\sim 18h^{-1}\text{Mpc}$ as being representative, $\Omega^{0.6}/b = 0.45 \pm 0.38$, where the quoted error is an average of the error bars in the $\sim 10\text{--}30h^{-1}\text{Mpc}$ region and is therefore the typical error on any *individual* point in this region. Naively combining the results in a maximum likelihood manner in the $\sim 10\text{--}20h^{-1}\text{Mpc}$ region gives an estimate of $\Omega^{0.6}/b = 0.48 \pm 0.11$. In this case the error estimate is likely to be slightly underestimated given the generally non-independent nature of ξ points. These results are discussed in more detail in Section 7 where comparisons with the results from structure formation models and other redshift surveys are made.

7 DISCUSSION

We now discuss the results obtained from the analysis presented in Sections 5 and 6. Given the observed problems with the unweighted estimate of ξ (Paper III), we now favour the weighted estimate of ξ in all of our analysis. This explains any slight numerical differences with respect to the quoted results of Ratcliffe et al. (1996a). However, we state clearly that our overall conclusions remain completely unchanged.

7.1 The One-Dimensional RMS Pairwise Velocity Dispersion

The minimum χ^2 fit of an exponential distribution function (with a streaming model) to the optimally estimated $\xi(\sigma, \pi)$ from the Durham/UKST survey gave a value for the one-dimensional rms pairwise velocity dispersion of $416 \pm 36 \text{ km s}^{-1}$. We note that this quoted error is the formal error obtained from the χ^2 statistic. Therefore, it is likely to be slightly underestimated given the non-independent nature of ξ . Our observed value is of particular interest as recent estimates from new redshift surveys and the re-analysis of old redshift surveys have been measuring larger velocity dispersions than the canonical value of $340 \pm 40 \text{ km s}^{-1}$ found by Davis & Peebles (1983) from the CfA1 survey. For example, using the CfA2/SSRS2 survey, Marzke et al. (1995) find $540 \pm 180 \text{ km s}^{-1}$ and, using the Las Campanas survey, Lin et al. (1996) find $452 \pm 60 \text{ km s}^{-1}$. Also, Mo, Jing & Börner (1993) measured large variations ($200\text{--}1000 \text{ km s}^{-1}$) in the velocity dispersion for a number of samples of similar size to CfA1 and they show that the estimated velocity dispersion is sensitive to galaxy sampling, especially dominant clusters the size of Coma. This new estimate from the Durham/UKST survey is still on the slightly low side, supporting the old Davis & Peebles (1983) value, but is not inconsistent ($>3\sigma$) with any of these other measured values. When considering these values it is important to note that the Durham/UKST survey covers a volume $\sim 4 \times 10^6 h^{-3} \text{ Mpc}^3$, approximately twice that of the CfA2/SSRS2 survey and half that of the Las Campanas survey. Also, in an unbiased (COBE-normalised) CDM model, Marzke et al. (1995) estimated that the velocity dispersion would converge to 10% within a volume $\sim 5 \times 10^6 h^{-3} \text{ Mpc}^3$. Therefore, the measurement from the Durham/UKST survey is hopefully both believable and representative of the actual value in the Universe. Finally, we note that the Durham/UKST survey does not contain any extremely dominant clusters (of Coma-like size) and therefore will not be biased high by this.

The best estimate of the one-dimensional rms pairwise velocity dispersion from the SCDM and LCDM simulations was 980 and 835 km s^{-1} , respectively, obtained using an exponential distribution function. These estimates agree well with the actual value of the velocity dispersion measured directly from the N -body simulations. However, both of these values are inconsistent with the measured value from the Durham/UKST survey at high levels of significance. In fact, taking the most negative approach possible (i.e. using the individual mock catalogue velocity dispersion error bar), one still finds a significant rejection ($>3\sigma$) of both CDM models. However, it should be noted that a significant velocity bias, b_v , between the matter and galaxy velocity distribu-

tions ($b_v \sim 0.4$), see Couchman & Carlberg (1992), would allow consistent results between the models and the data. Also, this rejection of the CDM models assumes that the simple models of linear biasing used here (Bardeen et al. 1986) are an adequate description of the galaxy formation process.

7.2 Infall and $\Omega^{0.6}/b$

The best estimates of $\Omega^{0.6}/b$ from the Durham/UKST survey are 0.52 ± 0.39 for the $J_3(s)/J_3(r)$ method and 0.45 ± 0.38 for the $\tilde{\xi}_2/\tilde{\xi}_0$ method, where we have (conservatively) quoted the estimate at one separation only. Given the integration procedure involved in the J_3 method we do not attempt to combine these points. However, naively combining the ξ_2/ξ_0 estimates gives $\Omega^{0.6}/b = 0.48 \pm 0.11$. This error is likely to be slightly underestimated given the non-independent nature of ξ . Our estimates can be compared with other *optical* values of $\Omega^{0.6}/b$ estimated using similar methods involving redshift space distortions. Peacock & Dodds (1994) use the real and redshift space power spectrum estimates of various cluster, radio, optical and IRAS samples to measure $\Omega^{0.6}/b = 0.77 \pm 0.16$. Loveday et al. (1996) use the J_3 method to measure $\Omega^{0.6}/b = 0.48 \pm 0.12$ for the APM-Stromlo survey. Lin et al. (1996) use the $\tilde{\xi}_2/\tilde{\xi}_0$ method to measure $\Omega^{0.6}/b = 0.5 \pm 0.25$ for the Las Campanas survey.

As one can see, all these observed values of $\Omega^{0.6}/b$ are consistent with ~ 0.5 . Therefore, using two fiducial values for b , $b = 1$ implies and the universe is open, $\Omega \sim 0.3$, and $b \sim 2$ implies the universe has the critical-density, $\Omega = 1$.

Finally, we state that our $\Omega^{0.6}/b$ estimates are consistent with those from the two CDM models of structure formation considered here (SCDM and LCDM). However, given that these models predict $(\Omega^{0.6}/b) \sim 0.4-0.6$ we are unable to distinguish between them.

8 CONCLUSIONS

We have investigated the redshift space distortions in the Durham/UKST Galaxy Redshift Survey using the 2-point correlation function perpendicular and parallel to the line of sight, $\xi(\sigma, \pi)$. On small, non-linear scales we observe an elongation of the ξ contours in the line of sight direction, which is due to the velocity dispersion of galaxies in virial regions. This is the common ‘‘Finger of God’’ effect seen in redshift surveys. On larger, linear scales we observe a compression of the ξ contours in the line of sight direction, which is due to the infall of galaxies into overdense regions.

We attempt to estimate the real space 2-point correlation function by direct inversion of the projected correlation function. We use two different inversion methods, Abel inversion and a new application of the Richardson-Lucy technique. We have tested these methods on mock catalogues drawn from cold dark matter (CDM) N -body simulations and find that they reproduce the correct answer. We apply the methods to the Durham/UKST survey and estimate $\xi(r)$. We find that a simple power law model gives best fit real space parameters of the correlation length, $r_0 = 4.8 \pm 0.5h^{-1}$ Mpc for the Abel method and $r_0 = 4.6 \pm 0.3h^{-1}$ Mpc for the Richardson-Lucy method, and slope, $\gamma = 1.6 \pm 0.3$ for the Abel method and $\gamma = 1.6 \pm 0.1$

for the Richardson-Lucy method. Our estimate is consistent with those from other redshift surveys and with the inversion of the APM $w(\theta)$ by Baugh (1996).

We use standard modelling techniques (e.g. Peebles 1980) to estimate the one-dimensional rms pairwise velocity dispersion of galaxies in the Durham/UKST survey. These methods (which were again tested on the mock catalogues) give an estimate of $\langle w^2 \rangle^{1/2} = 416 \pm 36 \text{ kms}^{-1}$ on $\sim 1h^{-1}$ Mpc scales. This value agrees well with recent estimates from new redshift surveys and re-analysis of old redshift surveys (Markze et al. 1995; Lin et al. 1996; Mo et al. 1993), although our value is still consistent with the canonical value of Davis & Peebles (1983). We compare with the predictions of the standard CDM model (SCDM; $\Omega h = 0.5$ & $b = 1.6$) and the low density CDM model with a non-zero cosmological constant to ensure spatial flatness (LCDM; $\Omega h = 0.2$, $\Lambda = 0.8$ & $b = 1.0$). We find that our results are significantly ($>3\sigma$) below the estimates from these models (assuming that linear biasing applies) and therefore these models are inconsistent with the data in this context. This modelling also produces an estimate of the real space correlation length from the Durham/UKST survey of $r_0 = 4.6 \pm 0.2h^{-1}$ Mpc, which is very consistent with the previously quoted values.

We use the modelling techniques of Kaiser (1987) and Hamilton (1992) to estimate $\Omega^{0.6}/b$ from the Durham/UKST survey. We test the methods with the mock catalogues and find that consistent results can be obtained. The Durham/UKST survey results from the $\xi(s)/\xi(r)$ method are too noisy to obtain a useful answer. The $J_3(s)/J_3(r)$ method produces an estimate of $\Omega^{0.6}/b = 0.52 \pm 0.39$, where we quote the estimate (and error) at one point only ($\sim 20h^{-1}$ Mpc) due to the non-independent nature of the integration procedure. The $\tilde{\xi}_2/\tilde{\xi}_0$ method gives $\Omega^{0.6}/b = 0.45 \pm 0.38$ at $\sim 18h^{-1}$ Mpc, which is representative of the results on these scales. Naively combining the points in the range $\sim 10-20h^{-1}$ Mpc gives a maximum likelihood fit of 0.48 ± 0.11 , where the error is likely to be slightly underestimated due to the general correlated nature of ξ points. A comparison with other optical estimates of $\Omega^{0.6}/b$ from redshift space distortion methods gives very consistent results with a value of $(\Omega^{0.6}/b) \simeq 0.5$. This argues against an unbiased critical-density universe ($b = 1$ & $\Omega = 1$), instead favouring either an unbiased low density universe ($b = 1$ & $\Omega \sim 0.3$) or a biased critical-density universe ($b \sim 2$ & $\Omega = 1$). Also, given that both CDM models considered here predict $(\Omega^{0.6}/b) \sim 0.4-0.6$ we cannot use our $\Omega^{0.6}/b$ results to distinguish between them.

Overall, combining these results with those presented in Paper III, we find that the standard CDM model underpredicts our 2-point correlation function results at large scales and overpredicts the one-dimensional pairwise velocity dispersion at small scales. Therefore, our results argue for a model with a density perturbation spectrum more skewed towards large scales, such as a low Ω CDM model with a cosmological constant.

ACKNOWLEDGMENTS

We are grateful to the staff at the UKST and AAO for their assistance in the gathering of the observations. S.M. Cole,

C.M. Baugh and V.R. Eke are thanked for useful discussions and supplying the CDM simulations. AR acknowledges the receipt of a PPARC Research Studentship and PPARC are also thanked for allocating the observing time via PATT and for the use of the STARLINK computer facilities.

REFERENCES

- Bardeen J.M., Bond J.R., Kaiser N., Szalay A.S., 1986, *ApJ*, 304, 15
- Baugh C.M., 1996, *MNRAS*, 280, 267
- Baugh C.M., Efstathiou G., 1993, *MNRAS*, 265, 145
- Bean A.J., Efstathiou G., Ellis R.S., Peterson B.A., Shanks T., 1983, *MNRAS*, 205, 605
- Cole S.M., Fisher K.B., Weinberg D.H., 1994, *MNRAS*, 267, 785
- Collins C.A., Heydon-Dumbleton N.H., MacGillivray H.T., 1988, *MNRAS*, 236, 7P
- Collins C.A., Nichol R.C., Lumsden S.L., 1992, *MNRAS*, 254, 295
- da Costa L.N., Pellegrini P.S., Davis M., Meiksin A., Sargent W.L., Tonry J.L., 1991, *ApJS*, 75, 935
- Couchman H.M.P., Carlberg R.G., 1992, *ApJ*, 389, 453
- Davis M., Peebles P.J.E., 1983, *ApJ*, 267, 465
- Efstathiou G., in Lawrence A., ed., 3rd *IRAS*, Conference, London, Comets to Cosmology. Springer, Berlin, p. 312
- Efstathiou G., Davis M., Frenk C.F., White S.D.M., 1985, *ApJS*, 57, 241
- Eke V.R., Cole S.M., Frenk C.S., Navarro J.F., 1996, *MNRAS*, 281, 703
- Fairall A.P., Jones A., 1988, *Publ. Dept. Astr. Cape Town*, 10
- Gaztañaga E. & Baugh C.M., 1995, *MNRAS*, 273, 1P
- Hamilton A.J.S., 1992, *ApJ*, 385, L5
- Hamilton A.J.S., 1993, *ApJ*, 417, 19
- Kaiser N., 1987, *MNRAS*, 227, 1
- Lilje P.B., Efstathiou G., 1988, *MNRAS*, 231, 635
- Lin H., Kirchner R.P., Tucker D.L., Shectman S.A., Landy S.D., Oemler A., Schechter P.L., 1996, submitted to *ApJ*
- Loveday J., Efstathiou G., Peterson B.A., Maddox S.J., 1992, *ApJ*, 400, L43
- Loveday J., Maddox S.J., Efstathiou G., Peterson B.A., 1995, *ApJ*, 442, 457
- Loveday J., Efstathiou G., Maddox S.J., Peterson B.A., 1996, *ApJ*, 468, 1
- Lucy L.B., 1974, *AJ*, 79, 745
- Lucy L.B., 1994, *AA*, 289, 983
- Marzke R.O., Geller M.J., da Costa L.N., Huchra J.P., 1995, *AJ*, 110, 477
- Metcalfe N., Fong R., Shanks T., Kilkeny D., 1989, *MNRAS*, 236, 207
- Metcalfe N., Fong R., Shanks T., 1995, *MNRAS*, 274, 769
- Mo H.J., Jing Y.P., Börner G., 1993, *MNRAS*, 264, 825
- Parker Q.A., Watson F.G., 1995, in Maddox S.J., Aragón-Salamanca A., eds., 35th Herstmonceux Conf. Cambridge, Wide Field Spectroscopy and the Distant Universe. World Scientific, Singapore, p. 33
- Peacock J.A., Dodds S.J., 1994, *MNRAS*, 267, 1020
- Peebles P.J.E., 1980, *The Large-Scale Structure of the Universe*, Princeton Univ. Press, Princeton, NJ
- Peterson B.A., Ellis R.S., Efstathiou G.P., Shanks T., Bean A.J., Fong R., Zen-Long Z., 1986, *MNRAS*, 221, 233
- Ratcliffe A., Shanks T., Broadbent A., Parker Q.A., Watson F.G., Oates A.P., Fong R., Collins C.A., 1996a, *MNRAS*, 281, L47
- Ratcliffe A., Shanks T., Parker Q.A., Fong R., 1996b, submitted to *MNRAS*
- Ratcliffe A., Shanks T., Fong R., Parker Q.A., 1996c, submitted to *MNRAS* (Paper III)
- Richardson W.J., 1972, *J. Opt. Soc. Am.*, 62, 55
- Saunders W., Rowan-Robinson M., Lawrence A., 1992, *MNRAS*, 258, 134
- Shanks T., Bean A.J., Efstathiou G., Ellis R.S., Fong R., Peterson B.A., 1983, *ApJ*, 274, 529
- Shanks T., Hale-Sutton D., Fong R., Metcalfe N., 1989, *MNRAS*, 237, 589
- Tucker D.L., Oemler A.A., Shectman S.A., Kirshner R.P., Lin H., Landy S.D., Schechter P.L., 1996, preprint.